

AN ABSTRACT OF THE THESIS OF

Jessica R. Curtis for the degree of Master of Science in Radiation Health Physics presented on June 9, 2016.

Title: Special Nuclear Material Analysis Using Temporal Gamma-Ray Spectroscopy and Machine Learning Methods

Abstract approved:

Steven R. Reese

Following thermal neutron induced fission, supervised machine learning and temporal gamma-ray spectroscopy methods were used to identify differences in the delayed gamma-ray spectra of Pu-239 and U-235. The temporal gamma-ray spectroscopy method takes advantage of the time-dependent decay of fission products. Employing Spearman's rank-order correlation coefficient and without prior knowledge of peak locations or their associated energies, temporal behavior patterns characteristic of radioactive decay were identified within the complex fission product gamma-ray spectra below 3 MeV of Pu-239 and U-235. Individual rho (ρ_s) values and their respective differences ($\Delta\rho_s$) were used as a part of feature selection to identify channels with significant attributes used as "fingerprints" to create profiles for Pu-239 and U-235 which may be used for the identification of temporal behavior in an unknown sample. This method may be combined with additional machine learning techniques for future quantification of fissile material with the potential for similar accuracy and precision to previous temporal gamma-ray spectrometry methods.

© Copyright by Jessica R. Curtis

June 9, 2016

All Rights Reserved

Special Nuclear Material Analysis Using Temporal Gamma-Ray Spectroscopy and
Machine Learning Methods

by

Jessica R. Curtis

A THESIS

submitted to

Oregon State University

in partial fulfillment of
the requirements for the
degree of

Master of Science

Presented June 9, 2016

Commencement June 2017

Master of Science thesis of Jessica R. Curtis presented on June 9, 2016

APPROVED:

Major Professor, representing Radiation Health Physics

Head of the School of Nuclear Science and Engineering

Dean of the Graduate School

I understand that my thesis will become part of the permanent collection of Oregon State University libraries. My signature below authorizes release of my thesis to any reader upon request.

Jessica R. Curtis, Author

ACKNOWLEDGEMENTS

I would like to thank my advisor, Dr. Steve Reese, for giving me the opportunity to work on such a fascinating research project. I am extremely grateful for his guidance, endless knowledge and support throughout this project. I would also like to thank Electra Sutton for her time and commitment as well as her wealth of knowledge as all greatly impacted the success of this project. Finally, I would like to thank my family and friends for their neverending support, love and encouragement.

TABLE OF CONTENTS

	<u>Page</u>
1 Introduction	1
1.1 Nuclear Safeguards	3
1.2 Nondestructive Assay Techniques	4
1.2.1 Passive Interrogation	5
1.2.2 Active Interrogation	6
1.2.3 Delayed Gamma-Ray Detection	8
1.2.4 Temporal Gamma-Ray Spectrometry	9
1.3 Evaluation of Lower Energy Delayed Gamma Emissions	10
1.4 Machine Learning	11
1.5 Descriptive Statistics	13
1.6 Goal and Objectives	14
2 Materials and Methods	16
2.1 OSU TRIGA Reactor and Beam Port #4	16
2.2 Fast Rabbit Pneumatic Transfer System	18
2.3 Irradiation of Samples	20
2.4 Gamma-Ray Spectroscopy	21
2.5 High-Purity Germanium Detector	21
2.6 List Mode	23
2.7 Parse Code	25
2.8 R Statistical Software	26
2.9 Descriptive Statistics	26
2.9.1 The Pearson Product-Moment Correlation Coefficient	27
2.9.2 Spearman's Rank-Order Correlation Coefficient	28

TABLE OF CONTENTS (continued)

	<u>Page</u>
2.10 Supervised Machine Learning	32
2.11 Use of Spearman’s Correlation Coefficient to Identify Patterns in Tem- poral Gamma-Ray Spectroscopy	33
2.12 Template Development	35
2.13 Quantiles	38
2.14 Evaluation Using R	39
 3 Results and Analysis	 43
3.1 Decay Template Sensitivity Analysis	43
3.2 Evaluation of Cycle Independence	45
3.3 Validation of ρ_s Computation	47
3.4 Frequency Quantile	51
3.5 Quantiles for $\Delta\rho_{s,HEU,Pu}$	52
3.5.1 Template 1 $\Delta\rho_{s,HEU,Pu}$ Quantiles	53
3.5.2 Template 2 $\Delta\rho_{s,HEU,Pu}$ Quantiles	58
3.5.3 Template 3 $\Delta\rho_{s,HEU,Pu}$ Quantiles	63
3.5.4 Template 4 $\Delta\rho_{s,HEU,Pu}$ Quantiles	68
3.6 Cycle Consistency	73
3.7 Identifying Significant Channels	74
3.7.1 The Relationship Between $\Delta\rho_{s,HEU,Pu}$ and ρ_s	75
3.8 Significant Channels	78
3.8.1 Template 1 Channel 139	79
3.8.2 Template 1 Channel 140	80
3.8.3 Template 1 Channel 230	81

TABLE OF CONTENTS (continued)

	<u>Page</u>
3.8.4 Template 1 Channel 301	82
3.8.5 Template 1 Channel 302	83
3.8.6 Template 1 Channel 964	84
3.8.7 Template 1 Channel 965	85
3.8.8 Template 3 Channel 1535	86
3.8.9 Template 3 Channel 1687	87
3.8.10 Template 3 Channel 1939	88
3.8.11 Template 3 Channel 2273	89
3.8.12 Template 4 Channel 231	91
3.8.13 Template 4 Channel 433	92
3.8.14 Template 4 Channel 834	94
3.8.15 Template 4 Channel 1503	95
3.8.16 Template 4 Channel 1628	96
3.8.17 Template 4 Channel 1787	97
4 Conclusion	101
5 Future Work	102

LIST OF FIGURES

<u>Figure</u>		<u>Page</u>
1	Thermal fission yield curves for Pu-239 (dashed line) and U-235 (solid line) (Chivers, 2011; England & Rider, 2011).	1
2	Horizontal section of the OSTR (Robinson, 2012).	16
3	Schematic of the PGNAA Facility Beam Port #4 (Robinson, 2012).	18
4	Schematic Cross Section of Beam Port #4 (Robinson, 2012).	18
5	Schematic of Fast Rabbit Pneumatic Transfer System#4 (Williford, 2013).	19
6	Photograph of Pu-239 (15.4 mg) sample.	20
7	Photograph of U-235 (178.2 mg) sample.	20
8	Schematic of three different coaxial geometries (Reproduced from Knoll, 2010).	22
9	Schematic of p- and n-type coaxial detectors. (Reproduced from Knoll, 2010).	22
10	Excerpt of <i>List Mode</i> text file from a 10 second HEU irradiation cycle produced by the ORTEC <i>ListDump</i> program.	24
11	Channel 230 Cycle 19 has a $\rho_{s,HEU}$ of 0.93, a $\rho_{s,Pu}$ of -0.47 and a $\Delta\rho_{s,HEU,Pu}$ of 1.40.	34
12	Channel 139 Cycle 5 has a $\rho_{s,HEU}$ of 0.95, a $\rho_{s,Pu}$ of -0.90 and a $\Delta\rho_{s,HEU,Pu}$ of 1.85.	35
13	Template displaying decay pattern.	36
14	Template displaying ingrowth pattern.	36
15	Template displaying ingrowth and decay pattern.	37
16	Template displaying decay and ingrowth pattern.	37
17	Plot of ρ_s versus per cent change in λ relative to Template 0.	45

LIST OF FIGURES (continued)

Figure		Page
18	Frequency of counts in each of the twenty cycles for the irradiation of HEU.	46
19	Frequency of counts in each of the twenty cycles for the irradiation of Pu.	46
20	The 98% $\Delta\rho_{s,HEU,Pu}$ quantile for Template 1 displaying channel frequency among cycles.	55
21	The 95% $\Delta\rho_{s,HEU,Pu}$ quantile for Template 1 displaying channel frequency among cycles.	56
22	The 90% $\Delta\rho_{s,HEU,Pu}$ quantile for Template 1 displaying channel frequency among cycles.	56
23	The 98% $\Delta\rho_{s,HEU,Pu}$ quantile for Template 2 displaying channel frequency among cycles.	60
24	The 95% $\Delta\rho_{s,HEU,Pu}$ quantile for Template 2 displaying channel frequency among cycles.	61
25	The 90% $\Delta\rho_{s,HEU,Pu}$ quantile for Template 2 displaying channel frequency among cycles.	61
26	The 98% $\Delta\rho_{s,HEU,Pu}$ quantile for Template 3 displaying channel frequency among cycles.	65
27	The 95% $\Delta\rho_{s,HEU,Pu}$ quantile for Template 3 displaying channel frequency among cycles.	66
28	The 90% $\Delta\rho_{s,HEU,Pu}$ quantile for Template 3 displaying channel frequency among cycles.	66
29	The 98% $\Delta\rho_{s,HEU,Pu}$ quantile for Template 4 displaying channel frequency among cycles.	69

LIST OF FIGURES (continued)

Figure		Page
30	The 95% $\Delta\rho_{s,HEU,Pu}$ quantile for Template 4 displaying channel frequency among cycles.	70
31	The 90% $\Delta\rho_{s,HEU,Pu}$ quantile for Template 4 displaying channel frequency among cycles.	70
32	Channel 139 Cycle 5 has a $\rho_{s,HEU}$ of 0.95, a $\rho_{s,Pu}$ of -0.90 and a $\Delta\rho_{s,HEU,Pu}$ of 1.85.	79
33	Channel 139 Cycle 11 has a $\rho_{s,HEU}$ of 0.62, a $\rho_{s,Pu}$ of -0.91 and a $\Delta\rho_{s,HEU,Pu}$ of 1.53.	79
34	Channel 140 Cycle 3 has a $\rho_{s,HEU}$ of 0.94, a $\rho_{s,Pu}$ of -0.79 and a $\Delta\rho_{s,HEU,Pu}$ of 1.73.	80
35	Channel 140 Cycle 9 has a $\rho_{s,HEU}$ of 0.85, a $\rho_{s,Pu}$ of -0.82 and a $\Delta\rho_{s,HEU,Pu}$ of 1.67.	80
36	Channel 230 Cycle 1 has a $\rho_{s,HEU}$ of 0.98, a $\rho_{s,Pu}$ of -0.79 and a $\Delta\rho_{s,HEU,Pu}$ of 1.77.	81
37	Channel 230 Cycle 19 has a $\rho_{s,HEU}$ of 0.93, a $\rho_{s,Pu}$ of -0.47 and a $\Delta\rho_{s,HEU,Pu}$ of 1.40.	81
38	Channel 301 Cycle 11 has a $\rho_{s,HEU}$ of 0.90, a $\rho_{s,Pu}$ of -0.71 and a $\Delta\rho_{s,HEU,Pu}$ of 1.61.	82
39	Channel 301 Cycle 7 has a $\rho_{s,HEU}$ of 0.87, a $\rho_{s,Pu}$ of -0.86 and a $\Delta\rho_{s,HEU,Pu}$ of 1.73.	82
40	Channel 302 Cycle 4 has a $\rho_{s,HEU}$ of 0.58, a $\rho_{s,Pu}$ of -0.58 and a $\Delta\rho_{s,HEU,Pu}$ of 1.16.	83
41	Channel 302 Cycle 3 has a $\rho_{s,HEU}$ of 0.93, a $\rho_{s,Pu}$ of -0.63 and a $\Delta\rho_{s,HEU,Pu}$ of 1.56.	83

LIST OF FIGURES (continued)

Figure	Page
42	Channel 964 Cycle 3 has a $\rho_{s,HEU}$ 0.87, a $\rho_{s,Pu}$ of -0.77 and a $\Delta\rho_{s,HEU,Pu}$ of 1.64. 84
43	Channel 964 Cycle 10 has a $\rho_{s,HEU}$ of 0.63, a $\rho_{s,Pu}$ of -0.39 and a $\Delta\rho_{s,HEU,Pu}$ of 1.02. 84
44	Channel 965 Cycle 3 has a $\rho_{s,HEU}$ of 0.69, a $\rho_{s,Pu}$ of -0.18 and a $\Delta\rho_{s,HEU,Pu}$ of 0.87. 85
45	Channel 965 Cycle 20 has a $\rho_{s,HEU}$ of 0.87, a $\rho_{s,Pu}$ of -0.71 and a $\Delta\rho_{s,HEU,Pu}$ of 1.58. 85
46	Channel 1535 Cycle 11 has a $\rho_{s,HEU}$ of -0.34, a $\rho_{s,Pu}$ of 0.61 and a $\Delta\rho_{s,HEU,Pu}$ of 0.95. 86
47	Channel 1535 Cycle 6 has a $\rho_{s,HEU}$ of 0.13, a $\rho_{s,Pu}$ of -0.63 and a $\Delta\rho_{s,HEU,Pu}$ of 0.76. 87
48	Channel 1687 Cycle 2 has a $\rho_{s,HEU}$ of 0.74, a $\rho_{s,Pu}$ of -0.22 and a $\Delta\rho_{s,HEU,Pu}$ of 0.96. 87
49	Channel 1687 Cycle 5 has a $\rho_{s,HEU}$ of -0.65, a $\rho_{s,Pu}$ of 0.17 and a $\Delta\rho_{s,HEU,Pu}$ of 0.82. 88
50	Channel 1939 Cycle 14 has a $\rho_{s,HEU}$ of 0.79, a $\rho_{s,Pu}$ of -0.05 and a $\Delta\rho_{s,HEU,Pu}$ of 0.84. 88
51	Channel 1939 Cycle 5 has a $\rho_{s,HEU}$ of -0.61, a $\rho_{s,Pu}$ of 0.40 and a $\Delta\rho_{s,HEU,Pu}$ of 1.01. 89
52	Channel 2273 Cycle 18 has a $\rho_{s,HEU}$ of -0.71, a $\rho_{s,Pu}$ of 0.47 and a $\Delta\rho_{s,HEU,Pu}$ of 1.18. 89
53	Channel 2273 Cycle 2 has a $\rho_{s,HEU}$ of 0.63, a $\rho_{s,Pu}$ of -0.37 and a $\Delta\rho_{s,HEU,Pu}$ of 1.00. 90

LIST OF FIGURES (continued)

Figure		Page
54	Channel 231 Cycle 17 has a $\rho_{s,HEU}$ of -0.59, a $\rho_{s,Pu}$ of 0.55 and a $\Delta\rho_{s,HEU,Pu}$ of 1.14.	91
55	Channel 231 Cycle 8 has a $\rho_{s,HEU}$ of -0.52, a $\rho_{s,Pu}$ of 0.33 and a $\Delta\rho_{s,HEU,Pu}$ of 0.85.	91
56	Channel 433 Cycle 4 has a $\rho_{s,HEU}$ of 0.50, a $\rho_{s,Pu}$ of -0.40 and a $\Delta\rho_{s,HEU,Pu}$ of 0.90.	92
57	Channel 433 Cycle 12 has a $\rho_{s,HEU}$ of 0.54, a $\rho_{s,Pu}$ of -0.46 and a $\Delta\rho_{s,HEU,Pu}$ of 1.00.	93
58	Channel 834 Cycle 11 has a $\rho_{s,HEU}$ of -0.52, a $\rho_{s,Pu}$ of 0.44 and a $\Delta\rho_{s,HEU,Pu}$ of 0.96.	94
59	Channel 834 Cycle 18 has a $\rho_{s,HEU}$ of -0.49, a $\rho_{s,Pu}$ of 0.29 and a $\Delta\rho_{s,HEU,Pu}$ of 0.78.	94
60	Channel 1503 Cycle 15 has a $\rho_{s,HEU}$ of -0.24, a $\rho_{s,Pu}$ of 0.68 and a $\Delta\rho_{s,HEU,Pu}$ of 0.92.	95
61	Channel 1503 Cycle 2 has a $\rho_{s,HEU}$ of 0.04, a $\rho_{s,Pu}$ of -0.67 and a $\Delta\rho_{s,HEU,Pu}$ of 0.71.	96
62	Channel 1628 Cycle 10 has a $\rho_{s,HEU}$ of 0.63, a $\rho_{s,Pu}$ of -0.17 and a $\Delta\rho_{s,HEU,Pu}$ of 0.80.	96
63	Channel 1628 Cycle 14 has a $\rho_{s,HEU}$ of -0.58, a $\rho_{s,Pu}$ of 0.81 and a $\Delta\rho_{s,HEU,Pu}$ of 1.39.	97
64	Channel 1787 Cycle 7 has a $\rho_{s,HEU}$ of -0.70, a $\rho_{s,Pu}$ of 0.42 and a $\Delta\rho_{s,HEU,Pu}$ of 1.12.	97
65	Channel 1787 Cycle 13 has a $\rho_{s,HEU}$ of -0.34, a $\rho_{s,Pu}$ of 0.75 and a $\Delta\rho_{s,HEU,Pu}$ of 1.09.	98

LIST OF TABLES

<u>Table</u>	<u>Page</u>	
1	Example ranking of two data sets. The first ranked data set is Channel 231 from a single Pu irradiation cycle and is to be compared with the ranked data of Template 1, the second data set.	29
2	HEU raw time-stamped data for Cycle 10 after parsing. UTC Time represents the Coordinated Universal Time and the real time represents the time.	40
3	HEU temporal interval matrix for Cycle 10. Each channels counts were divided into ten, six second intervals accounting for the total counts acquired over the sixty second counting period.	40
4	Pu temporal interval matrix for Cycle 11 with decay $\rho_{s,Pu}$	41
5	HEU temporal interval matrix for Cycle 11 with decay $\rho_{s,HEU}$	41
6	ρ_s results based on per cent change in λ relative to Template 0.	44
7	Interval values for Templates 1-4.	47
8	Test data sets created from the four templates in Table 2.	48
9	The ρ_s values for Template 1, the template displaying a decay pattern.	48
10	The ρ_s values for Template 2, the template displaying an ingrowth pattern.	49
11	The ρ_s values for Template 3, the template displaying an ingrowth followed by decay pattern.	49
12	The ρ_s values for Template 4, the template displaying a decay followed by ingrowth pattern.	50
13	The $\Delta\rho_{s,HEU,Pu}$ ranges for each template and all three percentiles.	52
14	Total number of channels returned in each cycle for all three percentiles for Template 1.	54

LIST OF TABLES (continued)

<u>Table</u>	<u>Page</u>
15	Channels present in at least 80% of the cycles for the 98 th percentile for Template 1. 57
16	Channels present in at least 80% of the cycles for the 95 th percentile for Template 1. 58
17	Total number of channels returned in each cycle for all three percentiles for Template 2. 59
18	Channels present in at least 80% of the cycles for the 98 th percentile for Template 2. 62
19	Channels present in at least 80% of the cycles for the 95 th percentile for Template 2. 63
20	Total number of channels returned in each cycle for all three percentiles for Template 3. 64
21	Channels present in at least 30% of the cycles for the 98 th percentile for Template 3. 67
22	Channels present in at least 30% of the cycles for the 95 th percentile for Template 3. 67
23	Total number of channels identified in each cycle for all three percentiles for Template 4. 68
24	Channels present in at least 30% of the cycles for the 98 th percentile for Template 4. 71
25	Channels present in at least 30% of the cycles for the 95 th percentile for Template 4. 71
26	Percentage of channel frequency for all four templates. 73
27	Channels identified by Templates 1 and 2. 77

LIST OF TABLES (continued)

<u>Table</u>		<u>Page</u>
28	Channels identified by Template 3.	77
29	Channels identified by Template 4.	78

1 Introduction

Improving the methods used for detection and quantification of fissile material is essential to nuclear security and safeguards as special nuclear material (SNM) accountability, control, safety and security remain to be of great importance. With the continued expansion of the nuclear industry and the need for safe management of spent fuel, particularly knowledge of Pu-239 and U-235 content, improving existing nondestructive assay (NDA) techniques is imperative.

U-235 and Pu-239 have similar fission yield curves with the majority of fission fragments having a mass number of 94 and 140 (Shultis, 2008). Figure 1 shows the fission product yields from the thermal neutron induced fission of U-235 and Pu-239, where plutonium is shifted toward higher masses. The similarities in their fission yield curves presents a challenge when differentiating these materials in an unknown sample.

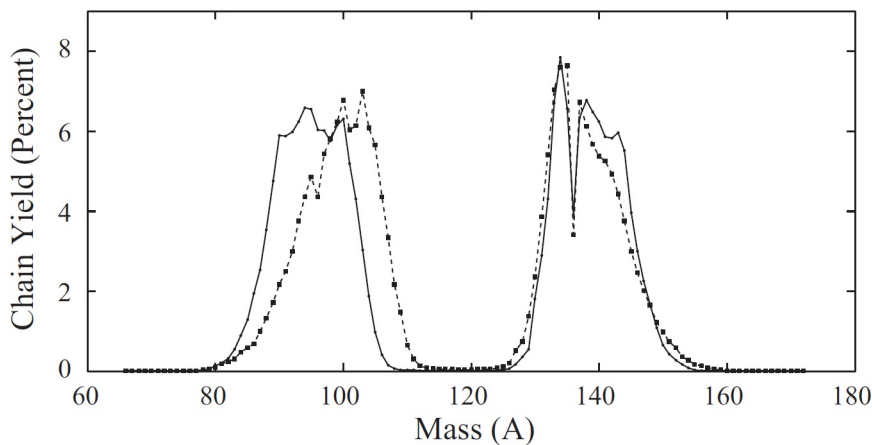


Figure 1: Thermal fission yield curves for Pu-239 (dashed line) and U-235 (solid line) (Chivers, 2011; England & Rider, 2011).

While passive measurements of special nuclear material have proven to be beneficial in certain situations, active interrogation methods such as thermal neutron induced fission followed by delayed gamma-ray detection have the ability to improve the detection and characterization of special nuclear material (Little, 2006). Traditionally, delayed gamma-ray detection has relied on peak identification and nuclear data in order to quantify fissile material. This process results in high uncertainties. Novel methods, such as temporal gamma-ray spectrometry, have been researched and suggest a reduction in the uncertainty associated with these traditional methods (Williford, 2013)

Williford's research in temporal gamma-ray spectrometry used the time-dependent decay characteristics of fission fragments to measure fissile material with improved accuracy and precision over traditional methods. Following thermal neutron induced fission, Williford evaluated the time and energy data of the resultant high energy beta-delayed gamma rays (≥ 3 MeV). Many of these well-developed peaks were composed of gammas from more than one fission product. Each of these fission fragment decay products had an individual half-life, yield and potential for ingrowth; therefore, they could be evaluated temporally. Williford looked not only at key peaks but at how those peaks changed as a function of time resulting in the identification and quantification of fissile material based on the temporal characteristics of these peaks.

The goal of this research is to explore whether using temporal spectroscopy methods and a nonparametric statistical method to evaluate the spectrum below 3

MeV will provide useful information that can be used for future quantification of fissile material with similar accuracy and precision.

1.1 Nuclear Safeguards

In 1968, the Nuclear Non-Proliferation Treaty (NNPT) was introduced and since then, 189 countries have signed. Under the IAEA, a safeguards system was established by the NNPT with the following goals: to prevent the spread of nuclear weapons and weapons technology, to promote the peaceful use of nuclear energy and to further disarmament (IAEA, 1970). To meet these goals, the nuclear industry has focused on proper management and accountability of nuclear materials, ensuring that the diversion of special nuclear material is detected in a timely manner, and deterring proliferation activities by making it known that detection is a possibility (Parker, 2015). Further, Physical Inventory Verification (PIV) tasks have been carried out by the IAEA to verify declared nuclear material inventories (Parker, 2015; Reilly, 1991). Nondestructive assay techniques are commonly used for the management and accountability of nuclear materials. These methods have been in use for decades and have become an integral part of nuclear safeguards.

1.2 Nondestructive Assay Techniques

Nondestructive assay techniques are categorized as either passive or active depending on whether they are used to measure the spontaneous or induced radiation emitted by nuclear materials (Reilly, 1991). Destructive analysis techniques require sampling and chemical analysis of the source material; whereas nondestructive assay techniques do not require the source material to be altered, physically or chemically. Nondestructive assay techniques are less time consuming and more cost effective than destructive analysis methods; however, they tend to be less accurate than chemical analysis (Reilly, 1991). To date, much research into the improvement and understanding of nondestructive assay techniques has been performed and the accuracy and precision of measurements has increased.

While the development of nondestructive assay methods occurred early on; it wasn't until the mid-sixties that the research and use of NDA techniques began to take off in the nuclear industry (Gozani, 1981). During this time the growth of the nuclear industry was at its highest and the need for more accurate measurements of nuclear materials for accountability and management was evident. Research into the use of passive and active nondestructive assay methods was performed at many of the national laboratories. Two of the main programs for active nondestructive assay were initiated under the Office of Safeguards and Material Management of the U.S. Atomic Energy Commission. In 1966, Los Alamos Scientific Laboratory researched using 14-MeV neutrons as a radiation source to perform active nondestructive assay

(Gozani,1981). In 1967, research on the use of high-energy gamma rays generated by a linear accelerator for active nondestructive assay was performed at the Linac Department of Gulf General Atomic (Gozani, 1981). Common applications of nondestructive assay include: accounting of nuclear material, searching for nuclear material as a safeguard against theft, verification of prior measurements and the quality control of nuclear materials (Gozani, 1981). Passive and active nondestructive assay techniques will be explored further in the next sections.

1.2.1 Passive Interrogation

Passive interrogation involves the detection of gamma rays emitted intrinsically from nuclear materials. Both, uranium and plutonium isotopes, emit alpha or beta radiation along with their associated gamma rays as a part of their natural decay process. In addition, both isotopes can spontaneously fission producing fission fragments along with their respective neutrons and gamma rays. The energies of the gamma rays emitted are characteristic of the nuclide from which they originated and detection of these gamma rays can be used to differentiate nuclear material from that of background (Reilly, 1991).

Gamma rays emitted naturally from U-235 and Pu-239 are typically low in energy, around the 500 keV range. For U-235, passive measurements include those at or below 186 keV and for Pu-239, those at or below 413 keV (Beddingfield and Cecil,1998). In most situations where uranium and plutonium need to be distinguished

from one another, these lower energies are difficult to detect due high background levels or to shielding. In addition, emissions from spontaneous fission are much lower than those from induced fission. Implementing active interrogation methods can overcome these challenges and results in a more accurate measurement of fissile material.

Passive interrogation is typically used to measure scrap, waste and residue; however, passive interrogation methods have their limits (Gozani, 1981). For instance, the emission of lower energy gamma rays from nuclear material such as uranium and plutonium are easily shielded making passive interrogation nearly impossible. Or, in the case of measuring plutonium and uranium in an spent nuclear fuel (SNF) assembly, a complex overlapping background exists from the gamma rays emitted by the build up of fission products during irradiation and those emitted by uranium and plutonium; making measuring these materials quite challenging using passive methods (Reilly, 1991).

1.2.2 Active Interrogation

The primary purpose for researching active NDA methods was for nuclear safeguards; however, improved processes for quality control also resulted (Gozani, 2009). Active interrogation involves the use of penetrating radiation, typically a photon or neutron source, to induce fission on fissile material resulting in fission fragments and their associated neutrons and gamma rays. Typically, a neutron source results in the prompt fission production of two to three neutrons and about eight gamma

rays (Gozani, 1981). Following irradiation, about six or seven delayed gamma rays are emitted and about 0.01 to 0.02 delayed neutrons per fission (Gozani, 1981).

Active interrogation techniques may be used to detect either the prompt or delayed emissions. On average, about eight photons are emitted per fission resulting in prompt gamma-ray emissions having strong signatures (Gozani, 2009). However, detecting the prompt emissions can be challenging due to irradiation and detection occurring simultaneously. Doing so requires implementing one of many methods in order to accurately differentiate the prompt fission emissions from the interrogating source (Gozani, 1981). Delayed emission detection on the other hand measures the decay of fission products after irradiation has ended. Inducing fission on U-235 and Pu-239 results in fission products that decay via beta decay resulting in the emission of subsequent gamma rays. Delayed gamma rays are about 500 to 700 times more intense than delayed neutrons from fission and therefore the counting of delayed gamma rays is a more sensitive method (Gozani, 1981).

Many authors have reported the use of active interrogation methods for detection and quantification of shielded SNM (Norman, 2004; Slaughter, 2005; Hall, 2007; Miller, 2013). In addition, significant research has been performed on using active interrogation for the management and accountability of Pu-239 and U-235 in spent fuel (Tobin, 2010; Rodriguez et al., 2013; Williford, 2013). Various active interrogation methods are being explored; however, one of the more common techniques utilizes the delayed gamma method.

1.2.3 Delayed Gamma-Ray Detection

Early research showed that differentiating U-235 from Pu-239 could be performed by using active interrogation and evaluating gamma-ray energy peaks greater than 800 keV by looking at their peak intensity ratios and comparing these values to calculated theoretical values (Beddingfield & Cecil, 1998). The intensity ratios were developed from the multiple isotopes comprising the chosen peaks and were independent of the number of fissions induced. While the authors confirmed that their method could be used to identify fissile material, they stated that a large number of intensity ratios needed to be evaluated to ensure accurate identification.

Firestone et al. extended this research and looked at the prompt and delayed gamma-rays in the 3-4 MeV range to determine concentration and enrichment of U-235. They found that the high-energy gamma rays above 3 MeV emitted from the decay of short-lived fission products which provide a unique signature of fissile material can be used to quantify uranium. Further, by using ratios of the gamma-ray intensities, the concentration of fission isotopes could be determined (Firestone et al, 2005).

Both of these approaches relied on nuclear data which carries fairly high uncertainty, especially for short-lived fission products. However, this research led to the identification of specific gamma-ray line pairs which dominated the gamma-ray spectrum from 1 minute to 14 hours following fission (Marrs et al., 2008). Marrs et al. focused on identifying gamma-ray line pairs that were insensitive to neutron

energy. They were able to identify line pairs and groups with intensity ratios that were different for U-235 and Pu-239 (Marrs et al, 2008). From here, research of a novel temporal gamma-ray spectroscopy method was explored empirically by Chivers (Chivers, 2011).

1.2.4 Temporal Gamma-Ray Spectrometry

In an effort to reduce the high uncertainties associated with traditional methods, Chivers suggested to only look at the temporal response from the beta-delayed gamma emissions of fissile materials. To do this, the peaks in the spectrum needed to be normalized so that only temporal differences were present. This was done by taking the counts in a 3 keV energy bin over a 2.5 second time frame and normalizing this by the total number of counts over a 10 second time frame (the entire counting interval) in the same 3 keV bin (Chivers, 2011). Using these ratios, characterization of fissile material could be performed and by taking the difference of these ratios the material could then be quantified. Chivers' work was promising but had not been carried out experimentally.

Building on their research, Williford exploited the time-dependent decay characteristics of fission fragments and evaluated not only the peaks but he also looked at how they changed as a function of time. To do this, Williford fission-normalized the measurements by using peak responses at a reference time and creating a continuous temporal spectrum. Several factors, such as the number of radioisotopes composing

the peak, their respective half-life as well as whether any of the radioisotopes experience ingrowth, influence the temporal response of peaks (Williford, 2013). The temporal method takes advantage of using the more pronounced, well-developed peaks composed of multiple fission fragments thus minimizing systemic biases. Through the evaluation of these high energy peaks (≥ 3 MeV) within the temporal spectrum, Williford showed that he could quantify fissile material with a 2 % uncertainty; a significant improvement from the existing 10 % uncertainty for SNF assemblies using traditional delayed gamma methods (Williford, 2013; Charlton, 2011).

1.3 Evaluation of Lower Energy Delayed Gamma Emissions

To present, the focus of research has been on higher energy delayed gamma rays that are easier to discern from the very complex spectrum of fission product delayed gamma emissions below 3 MeV. However, lower energy delayed gamma emissions are much more abundant. Evaluating the spectrum below 3 MeV using temporal methods paired with machine learning techniques and descriptive statistical methods leads to a data driven process that may provide additional information for fissile material identification within this overwhelming portion of the spectrum.

Given the unique time-dependent decay characteristics of fission products, known patterns of decay and ingrowth are expected throughout the spectrum. This a priori knowledge can be used to generate a training set of data which use patterns of decay and ingrowth to evaluate the spectra of uranium and plutonium. By learning

which temporal patterns are present and which channels have significant attributes in the spectra of uranium and plutonium, this information can be used as a set of rules to develop a model that can identify these same temporal patterns in an unknown sample.

1.4 Machine Learning

Machine learning is a subfield of computer science that originally was used for artificial intelligence. Through the use of algorithmic methods, machine learning is able to address complex data tasks. Breiman has written extensively about the two cultures of statistical modeling. Scientists either assume that data was created from a particular model or they assume an unknown model and apply algorithmic methods to the data to reach conclusions (Breiman, 2001). The latter ensures a data driven process and supports an innovative way of solving complex data problems.

Machine learning techniques are used across disciplines and have become increasingly used to solve the issues surrounding “big data”. Machine learning techniques, such as Neural Networks (NN) and Support Vector Machines (SVM), have been used to interpret gamma-ray spectrometry data (Yoshida et al., 2002; Dragovic et al., 2005; Kangas et al., 2008; Wei et al., 2010; Hata et al., 2015; Varley, 2016). For example, an artificial neural network (ANN) algorithm used for pattern recognition has been employed for gamma-ray spectral analysis from Ge detectors (Yoshida et al., 2002). Typically, ANN is rarely used for gamma-ray spectrometry analysis due to

the large spectral size (Yoshida et al., 2002). To overcome this, Yoshida et al. created a subset of data consisting of peak energy information as the input data and used patterns of emitted gamma-ray energies from individual nuclides for training. They were able to successfully use ANN for pattern recognition and identify radioisotopes within the gamma-ray spectra (Yoshida et al., 2002). However, they were unable to process the raw spectral data and were limited to a data set consisting of gamma-ray peak energies.

King states, "...the production of humanly comprehensible rules from a machine learning system allows the rules to be checked for consistency with existing knowledge and opens the possibility that rules may provide fresh insight." (King, 1992) King et al. used machine learning techniques to derive a set of rules that could be used to predict relative activities for two drugs.

In supervised machine learning, the use of background knowledge is important. A set of known inputs is used as a training set. These inputs are compared with the desired outputs given by a "teacher" with the goal of learning rules that map inputs to outputs. In our research, the inputs are rank-order, time-stamped data and templates displaying the natural relationships of ingrowth and decay seen in the emission of fission fragment decay products. The desired outputs are the rho scores computed by using Spearman's rank-order correlation coefficient (the measure of association between our templates and the trends occurring in the data). Employing these methods, allows the discovery of meaningful patterns within a large complex spectrum of gamma ray emissions.

1.5 Descriptive Statistics

Measures of correlation are descriptive statistical methods used to show the extent of relationship between two variables. Correlation measures are not used for inferential purposes; however, once a measure of correlation has been calculated, inferential statistics may be used to evaluate an hypothesis concerning the correlation (Sheskin, 2011). In addition, a correlation between two variables does not imply that a change in one variable causes a change in the other. If two variables have a strong correlation, one can not conclude that one variable caused a change in the other variable; rather it can be noted that there is an association present between the two variables (Mukaka, 2012). Two of the most common measures of correlation are the Pearson product-moment correlation coefficient (PPMCC) and the Spearman's rank-order correlation coefficient (Mukaka, 2012).

The Pearson product-moment correlation coefficient was developed by Karl Pearson in 1900 and is a measure of linear correlation between two values. Spearman's rank-order correlation coefficient was developed in 1904 by Charles Spearman and is a special case of the PPMCC. Spearman's rank-order correlation coefficient is used with rank-order data where PPMCC is used with interval/ratio data (Sheskin, 2011). Spearman's rank-order correlation coefficient evaluates the extent of a monotonic relationship between two variables. A monotonic increasing relationship exists if as one variable increase so does the other. A monotonic decreasing relationship exists if as one variable decreases (increases) the other increases (decreases) (Sheskin, 2011)

where the rate of change between variables does not necessarily occur at a constant rate; therefore, the relationship may be linear or curvilinear. A monotonic increasing relationship is indicative of a positive association whereas a monotonic decreasing relationship is indicative of a negative association (Sheskin, 2011).

The Spearman's method is ideal for data sets that do not have a normal distribution, have a potential for outliers and have non-linear relationships (Sheskin, 2011). Radioactive decay is a stochastic, non-linear process; making Spearman's rank-order correlation coefficient an appropriate method to implement into a machine learning process for the identification of the differences in the spectra of plutonium and uranium.

1.6 Goal and Objectives

The goal of this research project was to determine whether useful information could be obtained below 3 MeV from the fission product spectra of plutonium and uranium produced by thermal neutron induced fission through the use of supervised machine learning techniques and the application of nonparametric statistical methods. Typically, when performing active interrogation of SNM, the focus is placed on identifying peaks above 3 MeV as they provide a unique signature for fissile material and are easily discerned from background. The delayed gamma-ray spectrum below 3 MeV is quite complex making it difficult to identify peaks for characterizing SNM. Further, the fission yield curves of Pu-239 and U-235 overlap adding to the difficulty

in identifying these two materials independently.

By developing a data training set comprised of templates corresponding to known radioactive decay behavior and using Spearman's rank-order correlation coefficient, patterns can be identified within the gamma-ray spectra of uranium and plutonium. The result will be channels that show significant differences between the two materials. These significant attributes are characteristic of the radioactive decay behavior of the isotopes comprising these channels. The patterns and channels identified will therefore lead to a model that can be used for identification of unknown material.

The Prompt Gamma Neutron Activation Analysis Facility (PGNAA) is located at beam port #4, which penetrates the graphite reflector and looks directly at the core producing the highest thermal neutron flux of all the beam ports (Robinson, 2012; Williford, 2013). The facility consists of a collimator, beam shutter, sample chamber, beam stop and high purity germanium detector. The detector is housed within borated polyethylene and lead shielding and is positioned 90 degrees from the neutron beam. Lead and boral rings located in the collimator are used to collimate the neutron beam to a uniform diameter of 2 cm (Robinson, 2012). The beam is filtered by the use of bismuth and sapphire filters which reduce the gamma and fast neutrons, respectively. The shutter can be moved to prevent the neutron beam from entering the sample chamber when the beam port is not in use. The sample chamber is where the sample resides when it is undergoing irradiation. The beam stop is the final component of the PGNAA facility and is used to stop the beam when the shutter is open during irradiation. The facility components are designed so that they can be evacuated or back-filled with helium to reduce interactions with air that would increase background levels and decrease the signal-to-noise ratio of the detector (Robinson, 2012). Figures 3 and 4 show schematic diagrams of beam port #4.

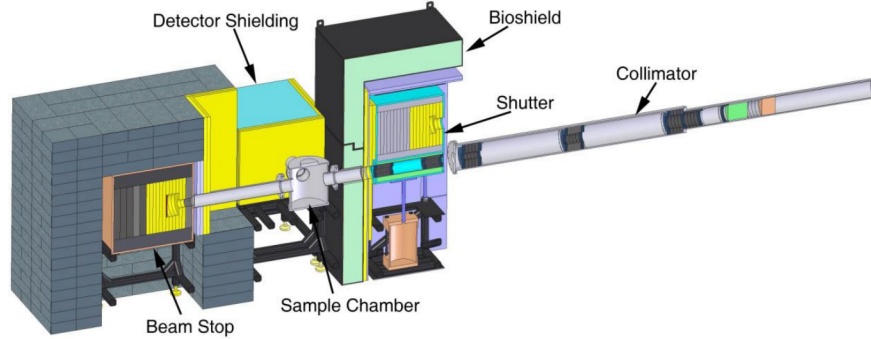


Figure 3: Schematic of the PGNAA Facility Beam Port #4 (Robinson, 2012).

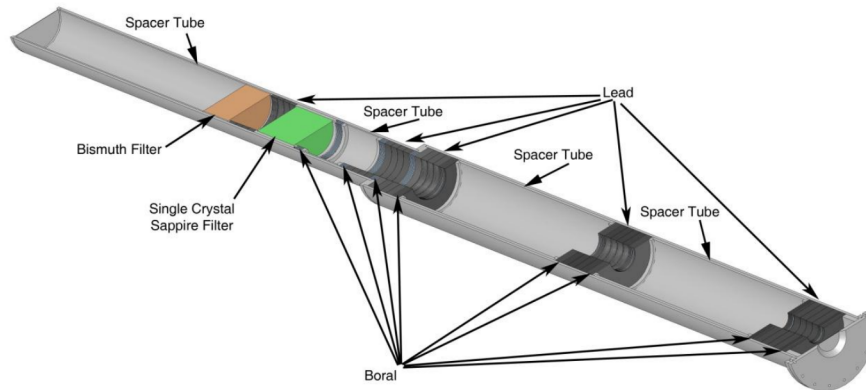


Figure 4: Schematic Cross Section of Beam Port #4 (Robinson, 2012).

2.2 Fast Rabbit Pneumatic Transfer System

A pneumatic transfer system was built around the PGNAA facility at the end of beam port #4 to maximize the counting geometry for samples. The original distance between the sample and the HPGGe detector when it was positioned 90 degrees from the neutron beam was about 30 cm; with the implementation of the new design,

the distance between the sample and the detector was 10 cm. This allowed for an ideal efficiency to look for low yield fission products from uranium and plutonium (Williford, 2013). The pneumatic transfer system was used to shuttle the sample between the beam and the detector. The polyethylene encapsulated sample was propelled through the system using pressurized helium with a transit time of 50 milliseconds (ms). A programmable logic controller (PLC) was setup to automate the irradiation time, count time and rest time. Two optical sensors were used to send a signal to the PLC indicating when the sample was being counted or irradiated. This information was then sent to the digital spectrometer where it was recorded in the *List Mode* data files. Figure 5 displays a schematic of the Fast Rabbit Pneumatic Transfer System.

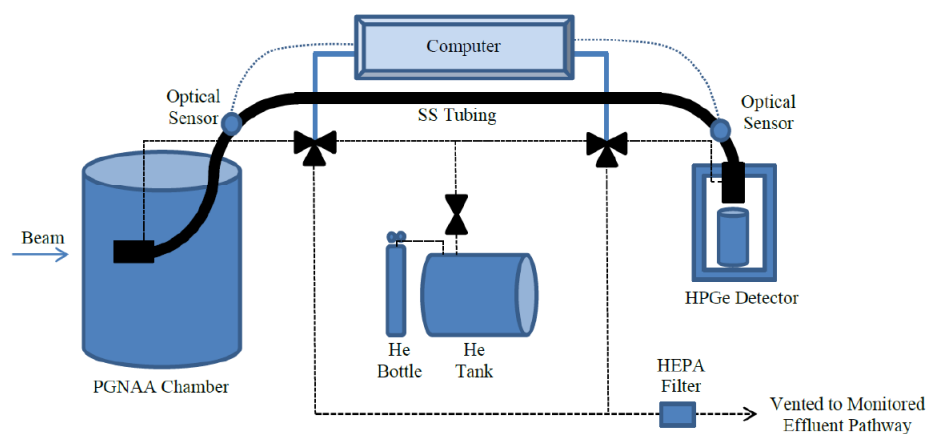


Figure 5: Schematic of Fast Rabbit Pneumatic Transfer System#4 (Williford, 2013).

2.3 Irradiation of Samples

Using beam port #4 and the fast rabbit pneumatic transfer system, samples of 178.2 milligrams (mg) of uranium-235 (HEU) nominally enriched to 93 % and 15.4 mg of plutonium-239 (Pu) were irradiated and counted in ten second, one minute and ten minute intervals for twenty cycles each. This research utilizes the temporal gamma-ray spectra data produced from the one minute irradiation cycles.



Figure 6: Photograph of Pu-239 (15.4 mg) sample.



Figure 7: Photograph of U-235 (178.2 mg) sample.

2.4 Gamma-Ray Spectroscopy

An important aspect of detection is understanding the way in which ionizing radiation interacts with matter. Charged particles, such as alpha and beta particles, interact directly with the material they are traversing via ionization or excitation. Photons on the other hand, are uncharged particles and interact indirectly with the material they pass through. Detection of these particles is dependent on the transfer of photon energy to electrons in the absorbing material. Three main interaction mechanisms are dominant in gamma-ray spectroscopy: photoelectric absorption, Compton scattering and pair production. Photoelectric absorption occurs most often for low-energy gamma rays, pair production occurs most often for high-energy gamma rays and Compton scattering occurs most often between these two extremes. The probability of occurrence of these three mechanisms is also dependent on the atomic number of the absorbing material. The probability of photoelectric absorption is greatest for high-Z materials and therefore gamma-ray spectroscopy detectors use materials with a high atomic number (Knoll, 2010).

2.5 High-Purity Germanium Detector

The detector used for this research was a coaxial, high-purity germanium detector (HPGe) chosen for its superior energy resolution. In a coaxial configuration, the core of the crystal is removed and one electrode is provided on the outer surface

(either p^+ or n^+ contact) of the crystal while a second electrode is provided on the inner surface (opposite contact of the outer electrode) of the crystal. Use of coaxial (cylindrical) geometry, incorporates a larger crystal volume resulting in a larger active volume in the detector (Knoll, 2010). Figure 8 displays the most common types of coaxial geometries and Figure 9 displays schematic diagrams of p- and n-type detectors.

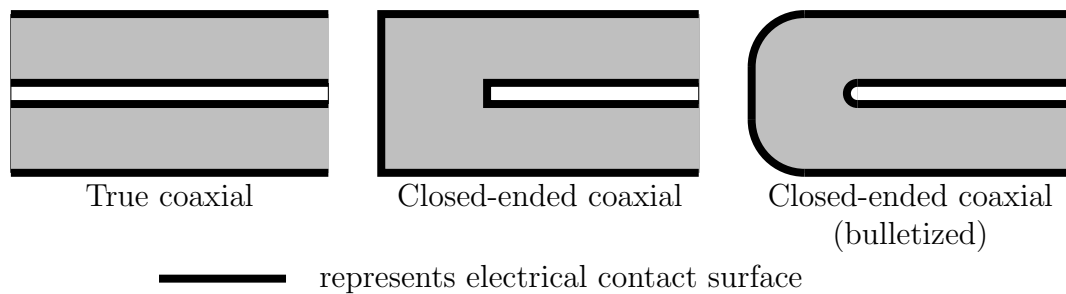


Figure 8: Schematic of three different coaxial geometries (Reproduced from Knoll, 2010).

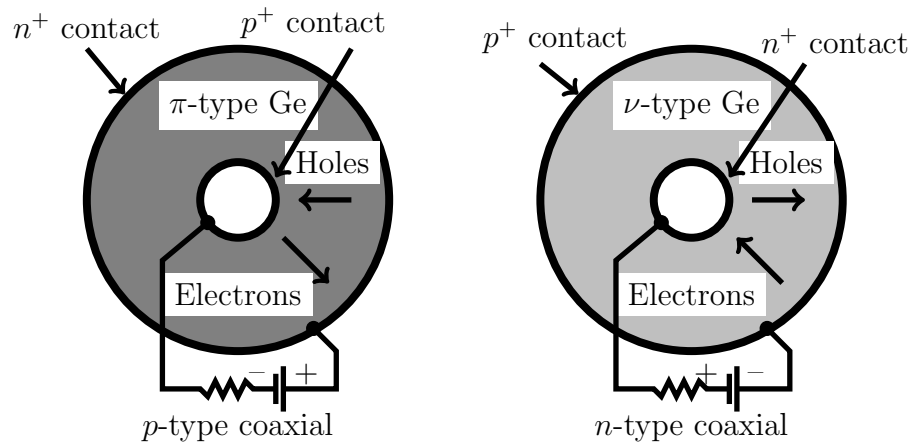


Figure 9: Schematic of p- and n-type coaxial detectors. (Reproduced from Knoll, 2010).

Semiconductors achieve better energy resolution due to the increased number of charge carriers for a given radiation event. In semiconductors, the carriers are electron-hole pairs moving between the valence and conduction bands of the crystal. In the presence of an applied electric field, these pairs move in opposite directions contributing to the conductivity of the material (Knoll, 2010). The small band gap between the valence and conduction bands of the semiconductor require that an HPGe detector must be cooled to liquid nitrogen temperature (77 K) to reduce current leakage so that the associated noise does not interfere with the energy resolution (Knoll, 2010). The HPGe detector was coupled with a digital spectrometer, the DSPEC Pro (Model: DSPEC Pro, Serial Number: 199), and can be operated in standard mode using GammaVision or in *List Mode* (ORTEC, 2016).

2.6 List Mode

Operating in *List Mode*, information such as the time of detection, energy channel, as well as live and real time data are collected and streamed to the computer (ORTEC, 2016). This data file can then be converted into a usable text file. For this research, the DSPEC Pro was operated in *List Mode* rather using traditional spectroscopy methods which result in a spectrum output for the user.

ListPRO is a program developed by ORTEC and is used to retrieve the *List Mode* data which is stored in an internal memory cache every 10 milliseconds (ORTEC, 2016). Following data retrieval, the cache is cleared and all data is dumped.

The result is a large data file (.dat) of each detected count, its respective time of occurrence (in increments of 200 nanoseconds), the channel in which the count occurred (ADC), running live and real time (in increments of 10 milliseconds), header information as well as external port readings (in increments of 10 milliseconds) that must be converted to a text file by the ORTEC *ListDump* program for further use (Williford, 2013).

The ORTEC *ListDump* program reads the .dat file and converts it to a tab delimited text file which displays a list of sequential events along with header information. Figure 10 shows an excerpt of the *List Mode* text file produced.

```

Source File:    HEU 6-26-14 10s(3).dat
Device Type:   DSPR-020
Device SN:     199
Start Date:    15:17:51 Thursday, June 26, 2014
Data Style:    DSPEC-PRO
Description:    HEU 10s irradiation, 10s count, no rest
Energy Cal:    0.138158 0.429014 -6.087e-008 keV
Shape Cal:     3.65436 0.00175951 -2.17623e-007
Conv. gain:    16384
Detector ID#:  3
Device Address: 131 1

U1      00000000: 0x018EA4C0
U2      00000001: 0x0291536A
U3      00000002: 0x030001CF      UTC Time: Thursday, June 26, 2014 15:29:27.308
                               Acq Start Reference: -160.1554 mS, Thursday, June 26, 2014 15:29:27.147
LT      00000003: 0x40000000      Live: 0.0000 mS
RT      00000004: 0x80000000      Real: 0.0000 mS      UTC Time: 15:29:27.147
CRM     00000005: 0x04000041      Cts/10 mS: 65
EX1     00000006: 0x05000000      Cts/10 mS: 0
EX2     00000007: 0x06000000      Cts/10 mS: 0
LT      00000008: 0x40000000      Live: 0.0000 mS
RT      00000009: 0x80000001      Real: 10.0000 mS      UTC Time: 15:29:27.157
CRM     00000010: 0x04000096      Cts/10 mS: 150
EX1     00000011: 0x05000000      Cts/10 mS: 0
EX2     00000012: 0x06000000      Cts/10 mS: 0
ADC     00000013: 0xC9A2119D      Real: 10.9018 mS      ADC: 2466      UTC Time: 15:29:27.158
ADC     00000014: 0xC0A923DA      Real: 11.8356 mS      ADC: 169      UTC Time: 15:29:27.159
ADC     00000015: 0xC1B43016      Real: 12.4620 mS      ADC: 436      UTC Time: 15:29:27.160
ADC     00000016: 0xC0BE3391      Real: 12.6402 mS      ADC: 190      UTC Time: 15:29:27.160
ADC     00000017: 0xC85D4BCC      Real: 13.8808 mS      ADC: 2141     UTC Time: 15:29:27.161
ADC     00000018: 0xC0405EF1      Real: 14.8610 mS      ADC: 64      UTC Time: 15:29:27.162
ADC     00000019: 0xC1328E8E      Real: 17.2988 mS      ADC: 306      UTC Time: 15:29:27.165
LT      00000020: 0x40000001      Live: 10.0000 mS

```

Figure 10: Excerpt of *List Mode* text file from a 10 second HEU irradiation cycle produced by the ORTEC *ListDump* program.

U1, U2 and U3 separate the Coordinated Universal Time (UTC) timestamps, the spectrometer's count-rate meter (CRM) records the time since the last cache dump, EX1 indicates the value of the signal into external port 1, ADC represents the channel in which the count was detected, LT represents the live time and RT represents the real time.

2.7 Parse Code

List Mode data was collected continuously during irradiation cycles whether the sample was in front of the detector or being irradiated. The *List Mode* data files needed to be parsed in order to evaluate the data when the sample was in front of the detector. To do this, Williford developed a parse code using Python. As mentioned earlier, in the *List Mode* text file the value of EX 1 represents where the sample is located. EX 1 has a value of 0 during sample irradiation and then switches to a value of 1 when the sample is at the detector. The parse code was written to look for the the switch from 0 to 1. Parsing of the raw data resulted in forty individual one-minute time stamped data files, twenty files corresponding to the twenty cycles of irradiation/counting performed for each material. These files contained the time at which a count was detected and the channel (ADC) in which it occurred.

2.8 R Statistical Software

R is a language and environment used for data calculation, manipulation and visualization (Venables et al., 2016). R has a history of being utilized for scientific and statistical analysis. It is available as Free Software through the GNU Operating System project. R contains many standard packages that make up the base environment. In addition to these, there are many packages available meant to extend the R environment (Venables et al., 2016). Lattice, a graphing package, was utilized for visualization of the temporal behavior present in channels of interest. The LOESS smoothing function was applied to the scatter plots to show the overall trend present in the data points. The LOESS method is used to fit a smooth curve between two variables. It is a nonparametric method of local polynomial regression. It is used as a non-formal modeling tool, as a scatter plot smoother (Avery, 2012).

2.9 Descriptive Statistics

Descriptive and inferential statistics are two areas that comprise the field of statistics. Descriptive statistics are referred to as assumption free and are used for presenting and summarizing data rather than for making predictions (Sheskin, 2011). Through the use of descriptive statistics, the data can be displayed in a meaningful way so that patterns may emerge. As mentioned earlier, evaluating the measures of association/correlation are categorized as descriptive statistical methods. In this

section, two measures of correlation will be discussed.

2.9.1 The Pearson Product-Moment Correlation Coefficient

The Pearson Product-Moment Correlation Coefficient (PPMCC) is a bivariate, parametric measure of association/correlation. This method is used with interval/ratio data to evaluate whether a linear relationship exists between two variables. The correlation coefficient computed by PPMCC is represented by the Greek letter rho, ρ and can have a value between 1 and -1. As the absolute value of ρ approaches 1, the strength of the linear relationship between the two variables increases (Sheskin, 2011). As the absolute value of ρ approaches 0, the strength of the linear relationship between the two variables decreases. The sign of ρ indicates the direction of the linear relationship where, a positive sign indicates a direct linear relationship and a negative sign indicates an indirect (inverse) linear relationship (Sheskin, 2011). The following formula is used to calculate ρ ,

$$\rho = \frac{\sum XY - \frac{(\sum X)(\sum Y)}{n}}{\sqrt{\left[\sum X^2 - \frac{(\sum X)^2}{n}\right] \left[\sum Y^2 - \frac{(\sum Y)^2}{n}\right]}} \quad (1)$$

where, X and Y represent the values of the two data sets, and n represents the number of measurements in the data set.

The PPMCC assumes a linear relationship best represents the data. The value of ρ may not indicate the extent of the relationship between the two variables if a

curvilinear relationship better describes the data (Sheskin, 2011). In this research, the temporal spectra were evaluated for curvilinear patterns of ingrowth and decay which are characteristic of radioactive decay. Spearman's rank-order correlation coefficient, used for curvilinear relationships, will be discussed next.

2.9.2 Spearman's Rank-Order Correlation Coefficient

Spearman's rank-order correlation coefficient is a nonparametric, descriptive statistical method used to investigate the strength of association between non-linear sets of rank-order data (Sheskin, 2011). Given that the Spearman's method assumes nothing about the distribution and is used for non-linear associations, it is an ideal method for use in this research. Spearman's rank-order correlation coefficient is a special case of the Pearson product-moment correlation coefficient therefore it is also represented by the Greek symbol rho, ρ , designated as ρ_s and referred to as Spearman's rho or Spearman's correlation coefficient. To calculate Spearman's correlation coefficient, the data sets are ranked separately in either ascending or descending order as long as the ranking is performed the same for both data sets (Sheskin, 2011). Table 1 shows an example of how two data sets would be ranked.

Channel Counts	Rank Pu-239	Template 1	Rank Template 1
264	10	659	1
267	9	435	2
283	7	287	3
275	8	190	4
285	6	125	5
295	4	83	6
287	5	54	7
306	2	36	8
301	3	24	9
313	1	16	10

Table 1: Example ranking of two data sets. The first ranked data set is Channel 231 from a single Pu irradiation cycle and is to be compared with the ranked data of Template 1, the second data set.

The difference in ranks is calculated, the resulting values squared and then summed. The following formula is used to calculate Spearman's correlation coefficient for untied ranks:

$$\rho_s = 1 - \frac{6 \sum_{i=1}^n (d_i)^2}{n(n^2 - 1)} \quad (2)$$

where, n represents the number of measurements in the data set and d_i represents the difference in ranks. While Equation 2 is for untied ranks, it has been noted in the literature that if only a few ties exist using Equation 2 is still quite reliable

(Brase, 1983). In R, a tie-corrected formula is used to compute Spearman's correlation coefficient. Equations 3 through 6 lead to the final formula utilized in R seen here as Equation 7:

$$T_x = \sum_{i=1}^s (t_{(x)}^3 - t_{i(x)}) \quad (3)$$

$$T_y = \sum_{i=1}^s (t_{(y)}^3 - t_{i(y)}) \quad (4)$$

The notations in Equations 3 and 4, indicate that for each variable, the number of tied ranks is subtracted from the number of tied ranks cubed and then summed.

$$\sum x^2 = \frac{n^3 - n - T_x}{12} \quad (5)$$

$$\sum y^2 = \frac{n^3 - n - T_y}{12} \quad (6)$$

where, n in Equations 5 and 6 represent the number of observations in the data set.

$$\rho_{s_c} = \frac{\sum x^2 + \sum y^2 - \sum d^2}{2\sqrt{\sum x^2 \sum y^2}} \quad (7)$$

In order to verify that the same ρ_s will be computed when using the tie-

corrected formula on data that are untied, consider a simple example where the computed Spearman's correlation coefficient is a value of one. Assume the sum of the difference in ranks to be zero and the number of observations in the data set to be ten. Substituting these values into Equation 2 computes the following ρ_s value:

$$\rho_s = 1 - \frac{6(0)}{10(10^2) - 1} = 1 \quad (8)$$

Now, compare the results from Equation 8 to the results of the tie-corrected formula used in R, Equation 11. Equations 3 and 4 result in a value of zero since there are no ties present in the data set. Substituting in ten for n and Equation 3 into Equation 5 the result is,

$$\sum x^2 = \frac{10^3 - 10 - 0}{12} = 82.5 \quad (9)$$

Substituting in ten for n and Equation 4 into Equation 6 the result is,

$$\sum y^2 = \frac{10^3 - 10 - 0}{12} = 82.5 \quad (10)$$

Finally, substituting in zero for the difference in ranks and Equations 5 and 6 into equation 7 the result is,

$$\rho_{s_c} = \frac{82.5 + 82.5 - 0}{2\sqrt{(82.5)x(82.5)}} = 1 \quad (11)$$

Equation 11 results in a Spearman's correlation coefficient of 1, the same result seen using Equation 8.

As with PPMCC, the Spearman's correlation coefficient produces a value between 1 and -1 indicating either a strong positive or a strong negative association between the paired data sets. As mentioned previously, an association between data sets does not imply causation (Sheskin, 2011). Spearman's rank-order correlation coefficient is a descriptive statistical method, and for the purposes of this research is used for pattern recognition, not to predict behavior.

2.10 Supervised Machine Learning

Supervised machine learning is driven by relationships. A rule based system is needed that uses known inputs and desired outputs to teach a system rather than to explicitly program it. Through feature selection, relevant features are identified in the data and used for model construction.

In this research, the known inputs are the interval ranked time-stamped data and templates whereas the desired outputs are the measures of association between the data sets, the ρ_s values. Signatures of nuclear material will be identified based on temporal behavior patterns. These relevant features are used to develop a model that

can be compared against an unknown data set to classify unknown nuclear material.

Through a library of templates, Spearman's rank-order correlation coefficient, a descriptive statistical method, can be used to identify temporal behavior patterns in the data. Once relevant features are selected the process can be automated and through the implementation of a decision tree, the classification of unknown special nuclear material can be performed. This process leads to a data driven method which supports forensic science.

2.11 Use of Spearman's Correlation Coefficient to Identify Patterns in Temporal Gamma-Ray Spectroscopy

This research employed a nonparametric statistical method as part of a supervised machine learning process to identify differences in the temporal gamma-ray spectra of uranium and plutonium. Typically, Spearman's correlation coefficient is used to determine whether or not an association between two random sets of paired data exists as part of a descriptive statistical process. For this research, Spearman's correlation coefficient was used for pattern identification as part of a machine learning process and therefore the Spearman's correlation coefficient computation was implemented in a slightly different way. While the raw time-stamped data sets of plutonium and uranium were random in nature due to the stochastic process of radioactive decay, they were compared individually to training data sets which were comprised of known inputs resembling specific patterns characteristic of radioactive decay in order

to tease out patterns in the plutonium and uranium temporal spectra. Comparing a random data set to one comprised of known inputs as a part of the supervised machine learning process made this method unique. Further, ρ_s for one channel/template pair of plutonium was compared to ρ_s of the same channel/template pair of uranium as opposed to evaluating ρ_s for the strengths of association between materials directly.

In order to determine which patterns were significant, delta rho ($\Delta\rho_{s,HEU,Pu}$) was calculated by taking the absolute value of the difference in the individual ρ_s values of plutonium and uranium. Implementing feature selection as part of the machine learning process, $\Delta\rho_s$ values were clustered to identify channels with the highest $\Delta\rho_s$ indicating those channels with the greatest difference between the two materials. For example, a channel that returns a “weak” ρ_s value for plutonium and a very “strong” ρ_s value for the same channel of uranium would result in a relatively large $\Delta\rho_s$ value indicating a difference in their temporal spectra as seen in Figure 11 below.

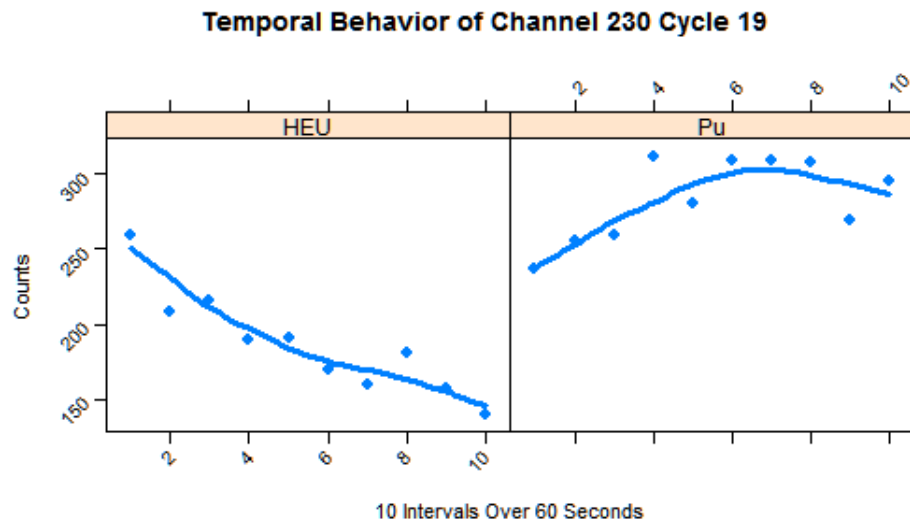


Figure 11: Channel 230 Cycle 19 has a $\rho_{s,HEU}$ of 0.93, a $\rho_{s,Pu}$ of -0.47 and a $\Delta\rho_{s,HEU,Pu}$ of 1.40.

Similarly, a channel that returns very “strong” ρ_s values for both plutonium and uranium but with opposite trends in association would also highlight the difference in temporal spectra between fissile materials and can be seen in Figure 12 below.

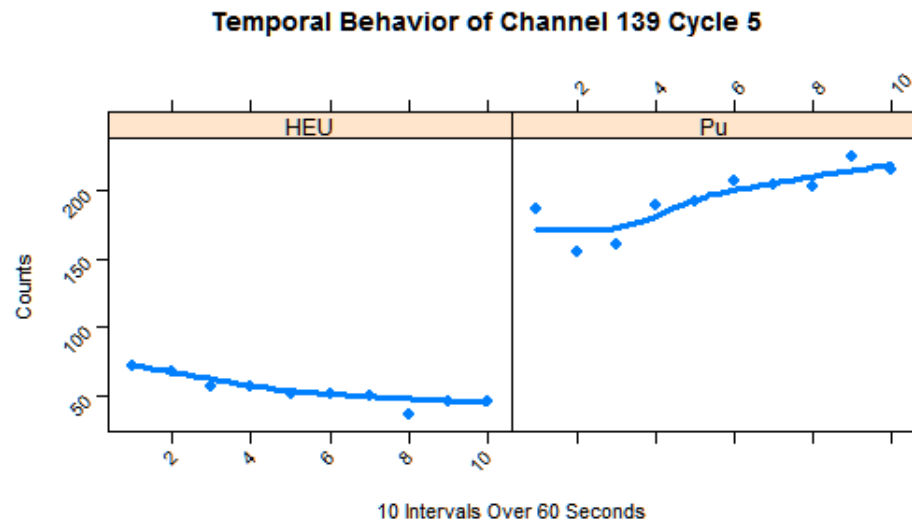


Figure 12: Channel 139 Cycle 5 has a $\rho_{s,HEU}$ of 0.95, a $\rho_{s,Pu}$ of -0.90 and a $\Delta\rho_{s,HEU,Pu}$ of 1.85.

Patterns such as these, highlight the differences in the temporal spectra of plutonium and uranium and help form a set of rules that may be implemented in the process of evaluating an unknown data set.

2.12 Template Development

Using the basic principles of the radioactive decay law and serial decay, four templates were created to form the training set of patterns to be used in the computation of Spearman’s correlation coefficient. In order to perform the computation of

Spearman's rho, the data sets being compared must have the same number of values. The sixty second counting cycles for each channel of the raw time-stamped data were divided into ten, six second intervals. Therefore, the templates used for the training set were developed to have ten, six second intervals as well.

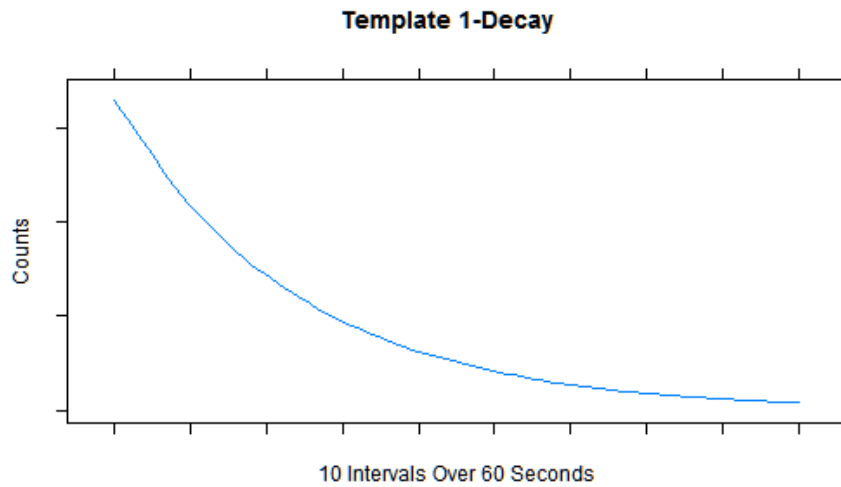


Figure 13: Template displaying decay pattern.

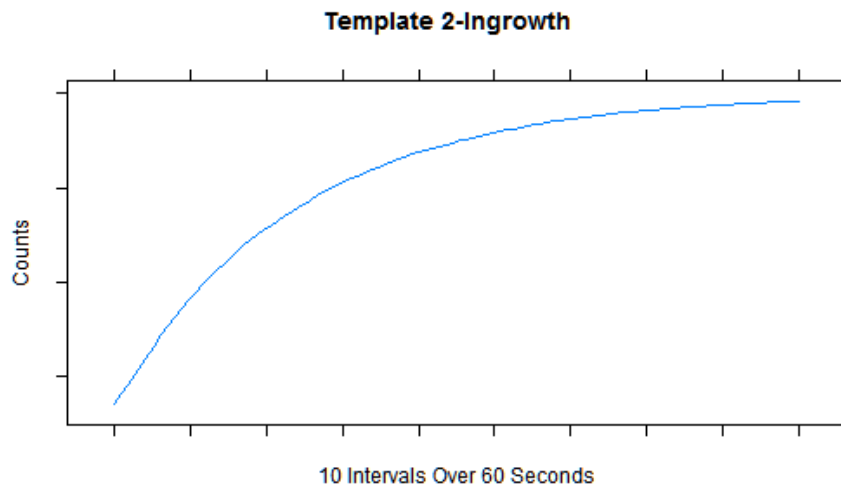


Figure 14: Template displaying ingrowth pattern.

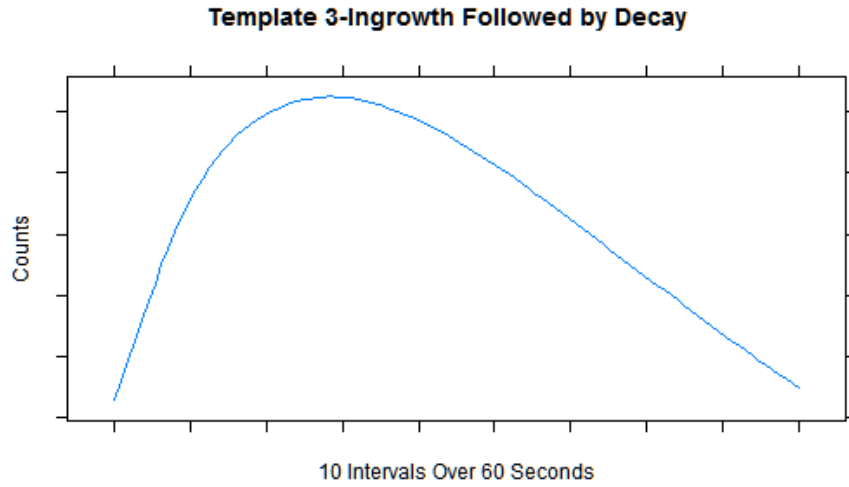


Figure 15: Template displaying ingrowth and decay pattern.

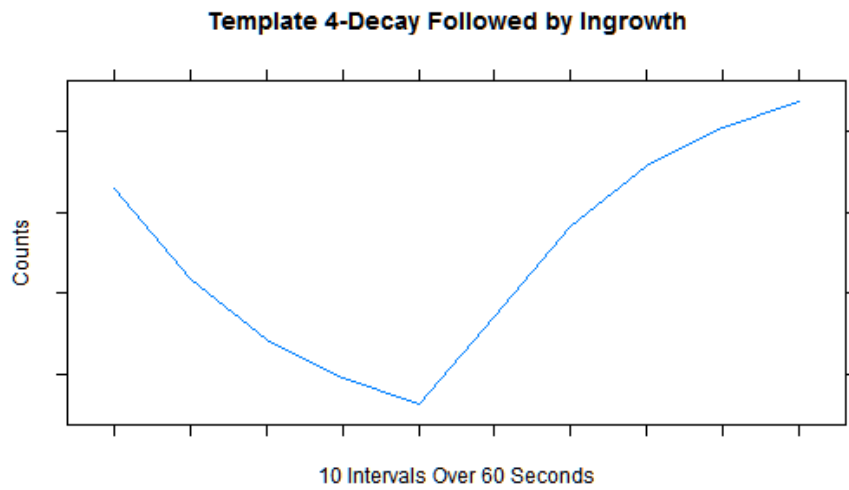


Figure 16: Template displaying decay and ingrowth pattern.

Positive and negative linear trend templates were not used. The results of the decay template sensitivity analysis, Section 3.1, showed that varying the decay rate of the function did not effect the ρ_s value. Even with a long decay rate, a near negative linear trend, the ρ_s value was still 1. For completeness, positive and negative

linear templates were created and run against the decay data. As expected, ρ_s values were -1 and 1, respectively.

2.13 Quantiles

A quantile is a measure used to divide a data set into equal percentage points (Sheskin, 2011). A percentile, an example of a quantile, corresponds to a value in the data set at which a certain percentage of the values fall at or below (Sheskin, 2011). The basic quantile function is described in R as,

```
quantile(x, probs = seq(0, 1, 0.25), na.rm = FALSE, names = TRUE, type = 7, ...)
```

where:

- *x*= data being measured
- *probs*=specifies the percentiles to be returned
- *na.rm*= a logical argument; if true, the NA values will be removed before the quantiles are computed.
- *names*=a logical argument; if true, the result has a names attribute
- *type*= an interger that identifies which of the nine quantile algorithms to be used

In R, the user has the ability to use the quantile function to cluster the data into various percentile groupings. The quantile function was utilized as a clustering technique at two different stages during the data analysis process; to remove the channels with the lowest count frequency and to determine significant channels based on the $\Delta\rho_{s,HEU,Pu}$ values.

2.14 Evaluation Using R

For initial proof-of-concept, individual channels from temporal gamma-ray spectra of uranium and plutonium were evaluated using a nonparametric, descriptive statistical method in R. In order to compute Spearman's correlation coefficient, temporal interval matrices for each cycle needed to be created. Using the parsed raw time-stamped data, the cut function in R was used to divide the time field into a sequence of ten, six second intervals for each cycle. The result was a temporal interval matrix of all channels for each cycle. Table 2 is an excerpt of the HEU raw time-stamped data after parsing of the *List Mode* data and before applying the cut function in R. Table 3 is an excerpt of the resulting temporal interval matrix for HEU.

Cycle	Real Time	Channel	UTC Time
10	1144530	1872	15:59:04.402
10	1144530	228	15:59:04.402
10	1144530	557	15:59:04.403
10	1144530	493	15:59:04.403
10	1144530	356	15:59:04.403
10	1144530	793	15:59:04.403
10	1144530	528	15:59:04.403
10	1144531	113	15:59:04.403
10	1144531	93	15:59:04.403
10	1144531	2945	15:59:04.404

Table 2: HEU raw time-stamped data for Cycle 10 after parsing. UTC Time represents the Coordinated Universal Time and the real time represents the time.

		Interval									
		1	2	3	4	5	6	7	8	9	10
Channel	338	48	50	50	49	38	48	48	36	47	39
	339	53	60	61	37	31	51	47	41	47	39
	340	58	71	58	46	47	36	41	43	37	34
	341	51	46	44	42	52	36	33	35	35	29

Table 3: HEU temporal interval matrix for Cycle 10. Each channels counts were divided into ten, six second intervals accounting for the total counts acquired over the sixty second counting period.

Using the quantile function in R, the channels with lower counts in the temporal interval matrices were removed. The 83rd percentile was used resulting in a unique count threshold of at least 100 counts to be applied to each cycle.

Using the training sets, Spearman’s correlation coefficient was computed for all forty cycles to identify patterns in the data that would show significant differences between HEU and Pu. Tables 4 and 5 are excerpts of the Pu and HEU interval matrices with their computed decay ρ_s , respectively.

		Interval										Decay
		1	2	3	4	5	6	7	8	9	10	$\rho_{s,Pu}$
Channel	301	162	194	189	174	197	205	202	206	226	194	-0.71
	302	186	223	205	177	192	233	228	218	213	232	-0.52
	303	181	172	174	167	155	193	164	191	197	173	-0.23
	433	102	86	66	76	60	62	76	53	60	57	0.81

Table 4: Pu temporal interval matrix for Cycle 11 with decay $\rho_{s,Pu}$.

		Interval										Decay
		1	2	3	4	5	6	7	8	9	10	$\rho_{s,HEU}$
Channel	301	108	97	75	72	67	57	47	43	40	57	0.90
	302	88	73	69	71	61	55	60	50	56	46	0.92
	303	94	81	72	77	70	43	59	53	54	55	0.81
	433	152	158	157	175	171	161	145	171	160	166	-0.30

Table 5: HEU temporal interval matrix for Cycle 11 with decay $\rho_{s,HEU}$.

The Pu and HEU interval matrices were then merged in order to calculate the $\Delta\rho_{s,HEU,Pu}$ values. This was repeated for each of the four templates comprising the data training set.

In order to determine significant channels within the data, the quantile function in R was utilized to cluster the data into various percentile groupings based on $\Delta\rho_{s,HEU,Pu}$ values. Based on the results, three percentiles (0.90, 0.95 and 0.98) were selected to evaluate channels identified as having significant differences for the two materials. Spreadsheets for all twenty cycles and each of the four templates were created for all three percentile groupings (0.90, 0.95 and 0.98). Histograms were used to visualize channel frequency across the twenty cycles. Subsets of channels with higher $\Delta\rho_{s,HEU,Pu}$ values that occurred consistently across cycles for each of the four templates were created for further evaluation. Lattice, a graphing package in R, was used to visualize the temporal behavior present in selected channels and to evaluate the differences between HEU and Pu.

3 Results and Analysis

3.1 Decay Template Sensitivity Analysis

Spearman's rank-order correlation coefficient is calculated by comparing the individual values of two sets of rank-order data against one another. Calculating the ρ_s based on rank-order implies that changes in the magnitude of the interval values within the data sets should not have an effect on the calculated ρ_s .

To determine whether varying the magnitude of the interval values of the template would have an effect on the calculated ρ_s , a sensitivity analysis was performed on the template displaying a decay pattern (Template 1), Figure 13. Using Template 1, a test data set of thirteen templates was created where Template 0 represents the original decay template with a decay constant (λ) of -0.0693. Twelve additional templates were created by varying λ in increments of +/- 10 % relative to template zero.

The Spearman's correlation coefficient calculation was performed on each of the thirteen template and test data template combinations. Table 6 shows the percent change in λ values calculated relative to Template 0 as well as the calculated ρ_s . As seen in Figure 17, varying the magnitude of the template did not have an effect on the ρ_s as it remained at a value of one (a perfect positive association) for each of the thirteen templates.

Based on these results, any of the thirteen templates could have been used to

identify the general decay pattern within the data. Template 1, the Decay Template with a λ of -0.0693 was chosen. As mentioned previously, Spearman's correlation coefficient is a descriptive statistical method, and in this research is used for pattern recognition, not to predict behavior.

Template	Per Cent Change Relative to Template 0	λ	ρ_s
0	0	-0.0693	1
1	-10%	-0.0624	1
2	+10%	-0.0762	1
3	-20%	-0.0554	1
4	+20%	-0.0832	1
5	-30%	-0.0485	1
6	+30%	-0.0901	1
7	-40%	-0.0416	1
8	+40%	-0.0970	1
9	-50%	-0.0347	1
10	+50%	-0.1040	1
11	-60%	-0.0277	1
12	+60%	-0.1109	1

Table 6: ρ_s results based on per cent change in λ relative to Template 0.

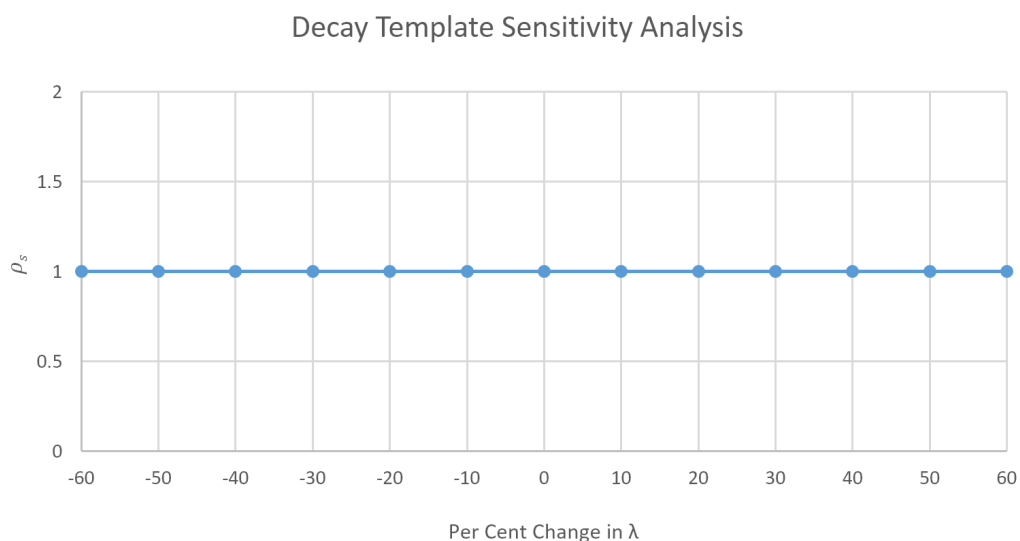


Figure 17: Plot of ρ_s versus per cent change in λ relative to Template 0.

3.2 Evaluation of Cycle Independence

Build-up of long-lived fission products occurs when the sample has not been given a long enough rest period before subsequent irradiations. In order to evaluate whether build-up was seen in the twenty cycles, a tally matrix was created for all channels across twenty cycles. The data was then plotted in Excel and a linear regression analysis was performed. The results indicated that both materials showed build-up; however, it was difficult to know where in the spectrum this was occurring. The trend lines in Figures 18 and 19 show a 10 %, a half per cent per cycle, increase in total counts from Cycle 1 to Cycle 20. The R^2 value for HEU is 0.15 and for Pu it is 0.81.

Build-up has the potential of obscuring peaks within the spectrum. In this research, evaluation of the spectrum was not based on identifying specific peaks. Rather, the entire spectrum was evaluated for patterns of radioactive decay and

ingrowth. Therefore, cycles were evaluated independently when determining the frequency and $\Delta\rho_{s,HEU,Pu}$ quantiles. Optimizing the irradiation and count/rest times could be beneficial at reducing the build-up seen and should be investigated as future work.

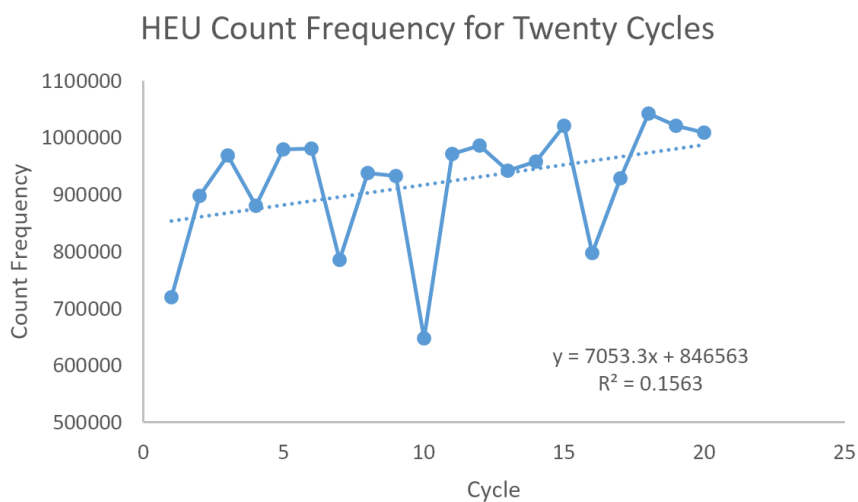


Figure 18: Frequency of counts in each of the twenty cycles for the irradiation of HEU.

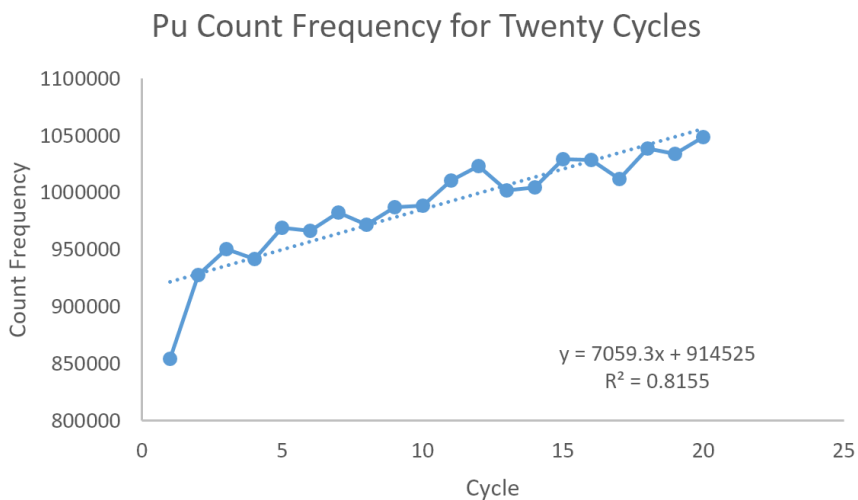


Figure 19: Frequency of counts in each of the twenty cycles for the irradiation of Pu.

3.3 Validation of ρ_s Computation

A simple analysis was performed in order to assess the accuracy of the calculation of Spearman's correlation coefficient using R. Test data sets were created by using the template values, seen in Table 7, and multiplying them by a factor of 3. This resulted in four test data sets, seen in Table 8, that when run against their corresponding template should return a ρ_s of 1. The Spearman's correlation coefficient computation was performed by running each of the four templates against the set of four test data sets. The subsequent ρ_s values were then evaluated and compared to the expected ρ_s values.

		Interval									
		1	2	3	4	5	6	7	8	9	10
Template	1	659	435	287	190	125	83	54	36	24	16
	2	340	565	713	810	875	917	946	964	976	984
	3	314	478	548	562	543	507	462	415	368	325
	4	659	435	287	190	125	340	565	713	810	875

Table 7: Interval values for Templates 1-4.

		Interval									
		1	2	3	4	5	6	7	8	9	10
Test Data	1	1977	1305	861	570	375	249	162	108	72	48
	2	1020	1695	2139	2430	2625	2751	2838	2892	2928	2952
	3	942	1434	1644	1686	1629	1521	1386	1245	1104	975
	4	1977	1305	861	570	375	1020	1695	2139	2430	2625

Table 8: Test data sets created from the four templates in Table 2.

		Interval										Template 1 ρ_s
		1	2	3	4	5	6	7	8	9	10	
Test Data	1	1977	1305	861	570	375	249	162	108	72	48	1.0
	2	1020	1695	2139	2430	2625	2751	2838	2892	2928	2952	-1.0
	3	942	1434	1644	1686	1629	1521	1386	1245	1104	975	0.32
	4	1977	1305	861	570	375	1020	1695	2139	2430	2625	-0.57

Table 9: The ρ_s values for Template 1, the template displaying a decay pattern.

Table 9 shows that when compared to the template displaying a decay pattern (Template 1), test data sets 1 and 2 resulted in a ρ_s of 1 and -1, respectively. This was expected as the values of test data set 1 showed a decay pattern while the values of test data set 2 showed an ingrowth pattern. Also expected, test data sets 3 and 4 had ρ_s values much lower than 1 and -1, respectively.

		Interval										Template 2 ρ_s
		1	2	3	4	5	6	7	8	9	10	
Test Data	1	1977	1305	861	570	375	249	162	108	72	48	-1.0
	2	1020	1695	2139	2430	2625	2751	2838	2892	2928	2952	1.0
	3	942	1434	1644	1686	1629	1521	1386	1245	1104	975	-0.32
	4	1977	1305	861	570	375	1020	1695	2139	2430	2625	0.57

Table 10: The ρ_s values for Template 2, the template displaying an ingrowth pattern.

Table 10 shows that when compared to the template displaying an ingrowth pattern (Template 2), test data sets 1 and 2 showed inverse results from that of the computation for the template displaying decay. Again, this was expected as the values of test data set 1 were of a descending order and the values of test data set 2 were of ascending order. Test data sets 3 and 4 also showed inverse results from that of the template displaying a decay pattern.

		Interval										Template 3 ρ_s
		1	2	3	4	5	6	7	8	9	10	
Test Data	1	1977	1305	861	570	375	249	162	108	72	48	0.32
	2	1020	1695	2139	2430	2625	2751	2838	2892	2928	2952	-0.32
	3	942	1434	1644	1686	1629	1521	1386	1245	1104	975	1.0
	4	1977	1305	861	570	375	1020	1695	2139	2430	2625	-0.89

Table 11: The ρ_s values for Template 3, the template displaying an ingrowth followed by decay pattern.

Table 11 shows that when compared to the template displaying an ingrowth followed by decay pattern (Template 3), test data set 3 was the only one to return a ρ_s value of 1. Test data sets 1 and 2 returned the same ρ_s value of 0.32 but with opposite signs and test data set 4 returned a ρ_s value of -0.89. Comparing Table 6 to Tables 4 and 5, test data sets 1 and 2 returned the same ρ_s values as test data set 3 returned when compared to the template displaying a decay pattern and the template displaying an ingrowth pattern.

		Interval										Template 4 ρ_s
		1	2	3	4	5	6	7	8	9	10	
Test Data	1	1977	1305	861	570	375	249	162	108	72	48	-0.57
	2	1020	1695	2139	2430	2625	2751	2838	2892	2928	2952	0.57
	3	942	1434	1644	1686	1629	1521	1386	1245	1104	975	-0.89
	4	1977	1305	861	570	375	1020	1695	2139	2430	2625	1.0

Table 12: The ρ_s values for Template 4, the template displaying a decay followed by ingrowth pattern.

Table 12 shows that when compared to the template displaying a decay followed by ingrowth pattern (Template 4), test data set 4 was the only data set to return a ρ_s value of 1. Test data sets 1 and 2 returned ρ_s values of -0.57 and 0.57, respectively. Test data set 3 returned a ρ_s value of -0.89. Comparing Tables 5 to 7, test data sets 1 and 2 returned the same ρ_s value of 0.57 (with opposite signs) as test data set 4 returned when compared to the template displaying a decay pattern and the template displaying an ingrowth pattern. Also, test data set 3 returned a ρ_s value

of -0.89 the same ρ_s value as test data set 4 returned when compared to the template displaying an ingrowth followed by decay pattern.

In summary, when the Spearman's correlation coefficient was computed on all of the test data set/training data set combinations, the expected ρ_s values were returned validating the accuracy of the Spearman's correlation coefficient computation in R.

3.4 Frequency Quantile

Using the quantile function in R, percentiles in one per cent increments ranging from 78 to 92 were evaluated. Counts varied across the twenty cycles for both materials. Rather than using a standard count threshold for all cycles, a percentile was chosen which resulted in using a count threshold that was unique to the individual cycle and material. The lowest count threshold for the entire percentile range (78 to 92) was 63 counts and the highest was 403.

After evaluating the data at each percentile, the 83rd percentile was chosen for the frequency quantile. This ensured that counts were greater than or equal to 100 for each of the twenty cycles and both materials. Choosing a count threshold of 100 resulted in the inclusion of the most channels that had the potential to be significant. Channels with counts lower than 100, on average, had less than 10 counts per interval which would not show enough variation in temporal behavior. The lowest count threshold for the 83rd percentile was 100 and the highest count threshold was

147. This shows that there was variation between materials and across the twenty cycles; however, the variation was minimal. Furthermore, the variation in counts at each percentile was typically within ten counts; the greatest variation being 31 counts for cycle 10 with HEU having 103 and Pu having 134. The 83rd percentile frequency quantile was held constant while the $\Delta\rho_{s,HEU,Pu}$ quantiles were varied.

3.5 Quantiles for $\Delta\rho_{s,HEU,Pu}$

The quantile function in R was also utilized as a clustering technique to determine significant channels based on the $\Delta\rho_{s,HEU,Pu}$ values. The 90th, 95th, and 98th percentiles were evaluated after performing the Spearman’s correlation coefficient computation for each of the templates comprising the training set. The $\Delta\rho_{s,HEU,Pu}$ values varied per cycle as well as template, resulting in a range of $\Delta\rho_{s,HEU,Pu}$ values at each percentile. Table 13 shows the $\Delta\rho_{s,HEU,Pu}$ ranges for each of the three percentiles.

		$\Delta\rho_{s,Pu,HEU}$ Percentile		
		0.90	0.95	0.98
Template	1	0.48-0.56	0.61-0.73	0.79-0.90
	2	0.48-0.56	0.61-0.73	0.79-0.90
	3	0.49-0.60	0.59-0.72	0.71-0.87
	4	0.53-0.64	0.66-0.76	0.79-0.92

Table 13: The $\Delta\rho_{s,HEU,Pu}$ ranges for each template and all three percentiles.

All three percentiles returned a significant number of channels for evaluation.

In order to determine which channels were consistently present within the twenty cycles, an output file of the frequency of channels present in each of the twenty cycles for all four templates was generated. To better visualize this information, histograms were created using MATLAB. The following section is divided into subsections which report the findings for each template that was a part of the training set used for evaluation. Templates 1 and 2 identified channels consistently across the cycles; therefore, channels were identified as significant if they were present in at least 80 % of cycles. Templates 3 and 4 identified channels with less consistency than Templates 1 and 2 but are included for completeness. Channels were selected as significant if they were present in at least 30 % of the cycles for these templates. Histograms of the 90th percentile were included for completeness; however, it was observed that while the overall number of channels identified increased, the channels which occurred with the most consistency displayed little variation. Therefore, the benefit of using the 90th percentile appeared minimal. Due to the abundance of channels returned and for the proof-of-concept of this research, focus was placed on comparing the 98th and 95th percentiles.

3.5.1 Template 1 $\Delta\rho_{s,HEU,P_u}$ Quantiles

Table 14 shows the number of channels identified in each cycle for all three percentiles for the template displaying a decay pattern (Template 1). The top 2 % of data returned 36 channels on average while the top 5 and 10 % returned 88 and 176

channels, respectively.

		$\Delta\rho_{s,HEU,Pu}$ Percentile		
		0.90	0.95	0.98
Cycle	1	168	87	34
	2	176	87	35
	3	175	91	36
	4	179	87	36
	5	174	93	37
	6	189	87	36
	7	173	87	37
	8	173	87	37
	9	179	87	35
	10	169	86	34
	11	176	91	35
	12	178	89	35
	13	182	89	35
	14	175	89	33
	15	174	91	35
	16	177	88	35
	17	178	88	39
	18	182	89	36
	19	175	88	36
	20	175	88	38

Table 14: Total number of channels returned in each cycle for all three percentiles for Template 1.

Figures 20 through 22 display histograms of the channel frequency throughout the twenty cycles for each of the three $\Delta\rho_{s,HEU,P_u}$ percentiles evaluated for Template 1. The total number of channels identified increased as the percentile of the $\Delta\rho_{s,HEU,P_u}$ quantile decreased; however, the frequency of the channels which occurred most often among the twenty cycles displayed little variation overall between the three percentiles.

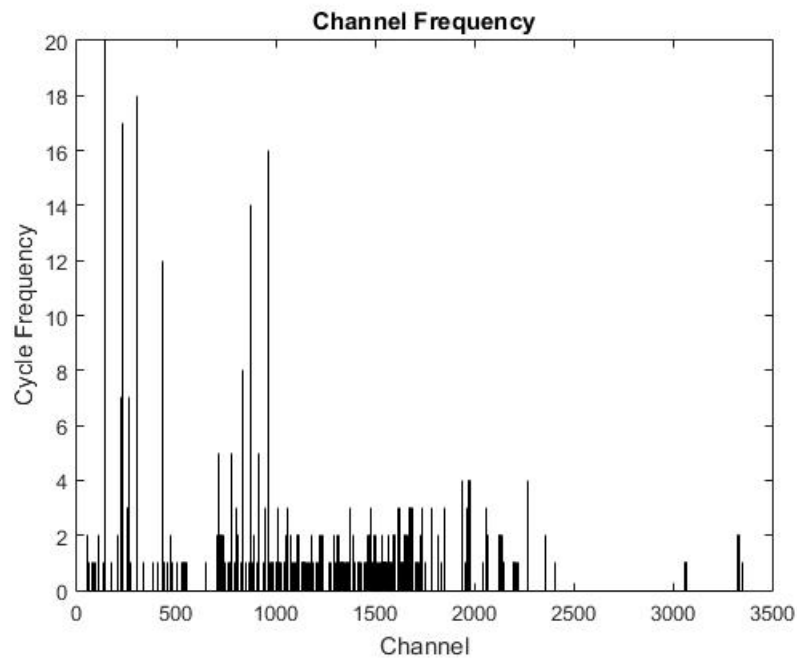


Figure 20: The 98% $\Delta\rho_{s,HEU,P_u}$ quantile for Template 1 displaying channel frequency among cycles.

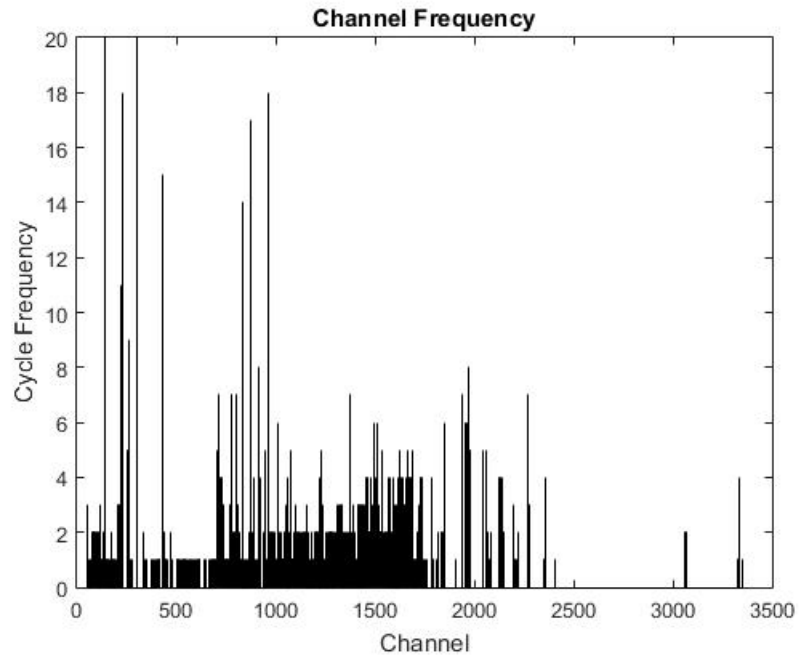


Figure 21: The 95% $\Delta\rho_{s,HEU,P_u}$ quantile for Template 1 displaying channel frequency among cycles.

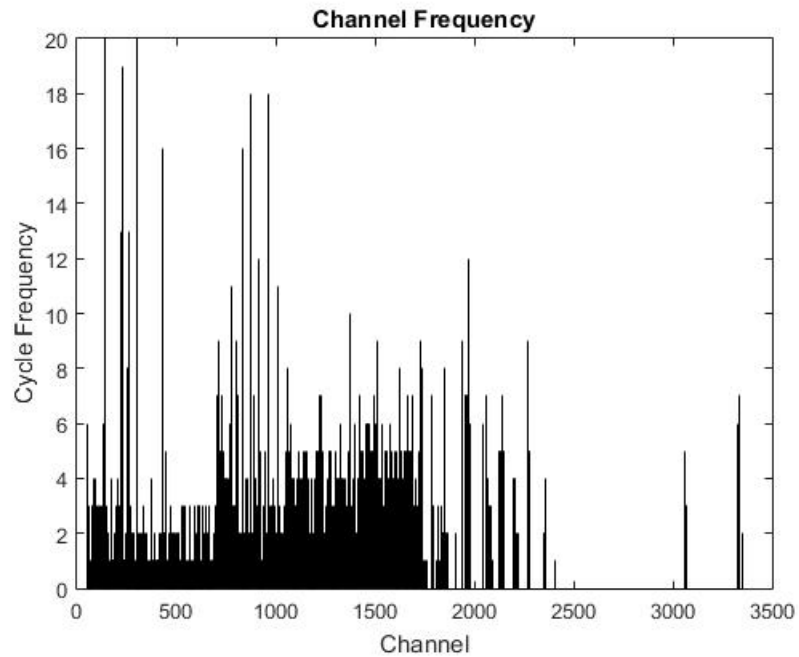


Figure 22: The 90% $\Delta\rho_{s,HEU,P_u}$ quantile for Template 1 displaying channel frequency among cycles.

There were several channels seen in all three percentiles consistently. These channels also had the most consistent showing across all twenty cycles. Tables 15 and 16 show the channels that occurred in at least 80% of the cycles for the 98th and the 95th percentiles, respectively. Table 16, shows that including the top 5 % of the data (a $\Delta\rho_{s,HEU,Pu}$ value of at least 0.70) resulted in the addition of three more channels and increased the overall consistency of previously identified channels among the twenty cycles.

Channel	Frequency	Percentage
139	20	100
140	18	90
230	17	85
301	17	85
302	18	90
965	16	80

Table 15: Channels present in at least 80% of the cycles for the 98th percentile for Template 1.

Channel	Frequency	Percentage
139	20	100
140	18	90
230	17	85
231	16	80
301	20	100
302	20	100
874	17	85
964	17	85
965	18	90

Table 16: Channels present in at least 80% of the cycles for the 95th percentile for Template 1.

3.5.2 Template 2 $\Delta\rho_{s,HEU,Pu}$ Quantiles

Template 2, the template displaying an ingrowth pattern, identified the same channels as Template 1; however, Template 2 returned inverse ρ_s values to that of Template 1. This is expected as the templates are inverse of one another. Table 17 below, shows the number of channels identified in each cycle for all three percentiles. The top 2 % of data returned 36 channels on average while the top 5 and 10 % returned 88 and 176 channels, respectively.

		$\Delta\rho_{s,HEU,Pu}$ Percentile		
		0.90	0.95	0.98
Cycle	1	168	87	34
	2	176	87	35
	3	175	91	36
	4	179	87	36
	5	174	93	37
	6	189	87	36
	7	173	87	37
	8	173	87	37
	9	179	87	35
	10	169	86	34
	11	176	91	35
	12	178	89	35
	13	182	89	35
	14	175	89	33
	15	174	91	35
	16	177	88	35
	17	178	88	39
	18	182	89	36
	19	175	88	36
	20	175	88	38

Table 17: Total number of channels returned in each cycle for all three percentiles for Template 2.

Figures 23 through 25 display histograms of channel frequency among the twenty cycles for each of the three $\Delta\rho_{s,HEU,Pu}$ percentiles evaluated for Template

2. Again, the total number of channels identified increased as the percentile of the $\Delta\rho_{s,HEU,P_u}$ quantile decreased; however, the frequency of the channels which occurred most often among the twenty cycles displayed little variation.

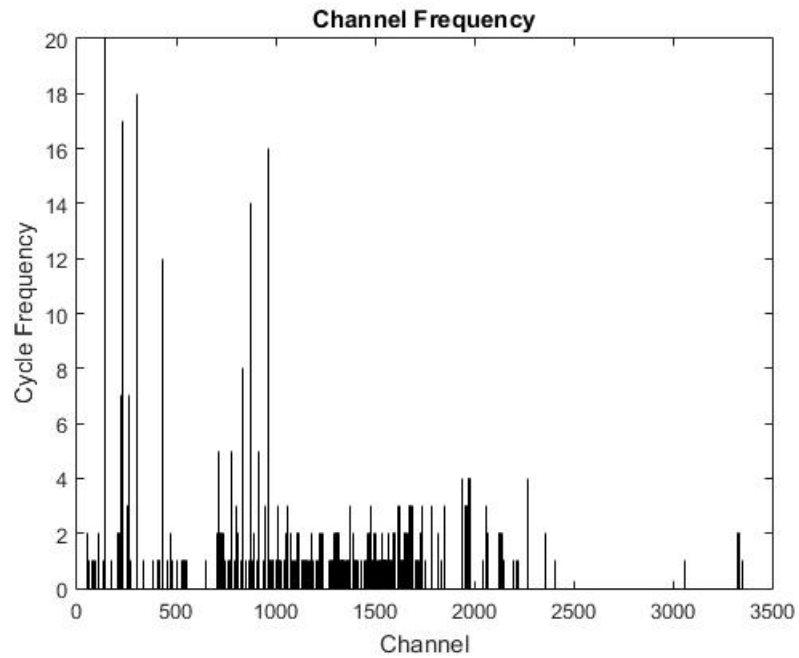


Figure 23: The 98% $\Delta\rho_{s,HEU,P_u}$ quantile for Template 2 displaying channel frequency among cycles.

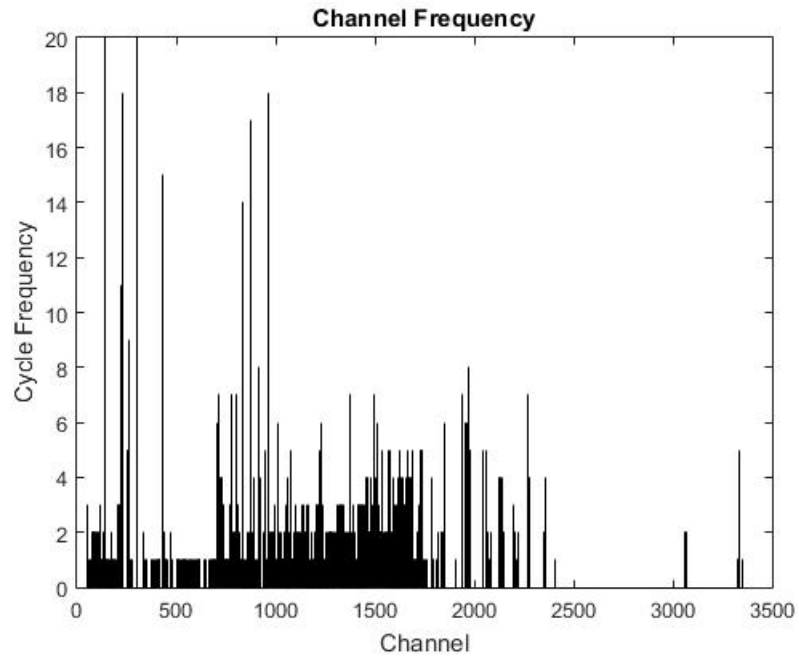


Figure 24: The 95% $\Delta\rho_{s,HEU,P_u}$ quantile for Template 2 displaying channel frequency among cycles.

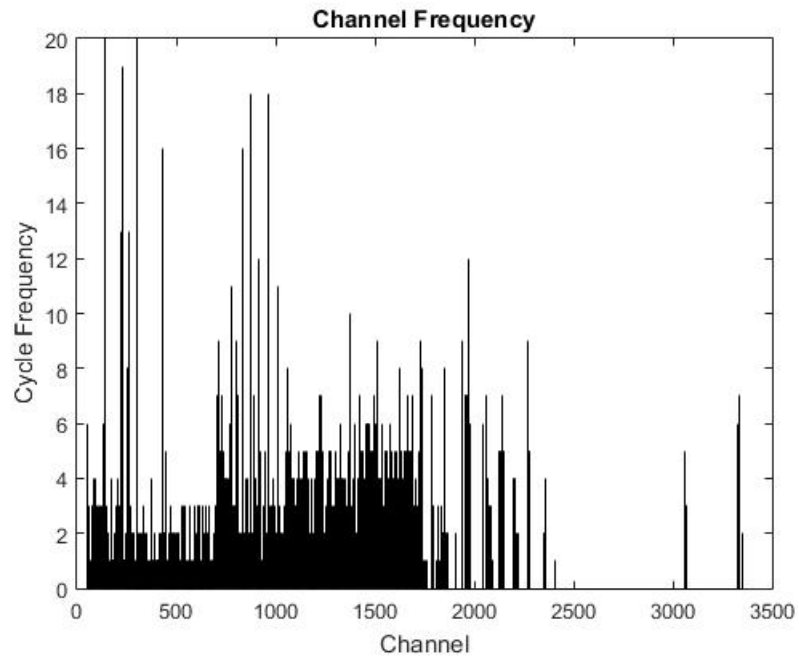


Figure 25: The 90% $\Delta\rho_{s,HEU,P_u}$ quantile for Template 2 displaying channel frequency among cycles.

Tables 18 and 19 show that the same channels were seen consistently throughout the twenty cycles for Template 2 as for Template 1. By moving from the 98th percentile to the 95th percentile, three additional channels were identified and the overall channel consistency among the twenty cycles increased.

Channel	Frequency	Percentage
139	20	100
140	18	90
230	17	85
301	17	85
302	18	90
965	16	80

Table 18: Channels present in at least 80% of the cycles for the 98th percentile for Template 2.

Channel	Frequency	Percentage
139	20	100
140	18	90
230	17	85
231	16	80
301	20	100
302	20	100
874	17	85
964	17	85
965	18	90

Table 19: Channels present in at least 80% of the cycles for the 95th percentile for Template 2.

3.5.3 Template 3 $\Delta\rho_{s,HEU,Pu}$ Quantiles

Table 20 shows the overall number of channels identified in each cycle by Template 3, the template displaying ingrowth followed by decay, for each percentile evaluated. The top 2 % of data returned 36 channels on average while the top 5 and 10 % of data returned 90 and 177, respectively.

		$\Delta\rho_{s,HEU,P_u}$ Percentile		
		0.90	0.95	0.98
Cycle	1	170	86	36
	2	179	91	35
	3	183	88	37
	4	175	91	36
	5	183	91	35
	6	186	91	39
	7	174	87	35
	8	184	90	36
	9	173	90	36
	10	171	89	34
	11	177	88	36
	12	177	97	36
	13	173	92	36
	14	175	89	37
	15	175	87	35
	16	177	87	36
	17	175	90	35
	18	174	93	36
	19	177	93	35
	20	179	90	35

Table 20: Total number of channels returned in each cycle for all three percentiles for Template 3.

Figures 26 through 28 display histograms of channel frequency among the twenty cycles for each of the three $\Delta\rho_{s,HEU,P_u}$ percentiles evaluated for Template 3.

As mentioned previously, the channels identified by Template 3 did not display the consistency seen by Templates 1 and 2 across the twenty cycles. Figure 26 shows that only two channels were seen in at least 30 % of the cycles for the 98th percentile. Figure 27 shows only one channel seen in at least 45 % of the cycles for the 95th percentile and Figure 28 shows that only one channel was seen in at least 50 % of the cycles for the 90th percentile. Due to this inconsistency, channels that were present in at least 30 % of cycles were included for evaluation.

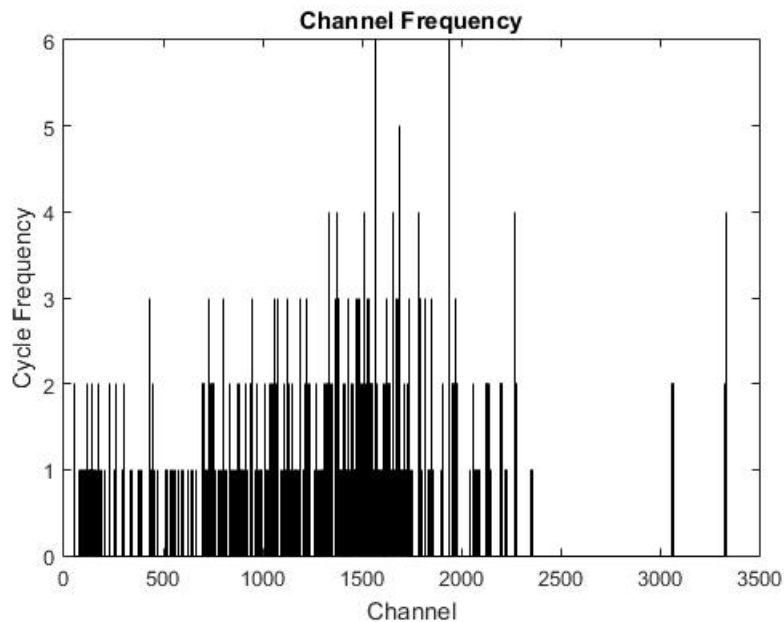


Figure 26: The 98% $\Delta\rho_{s,HEU,Pu}$ quantile for Template 3 displaying channel frequency among cycles.

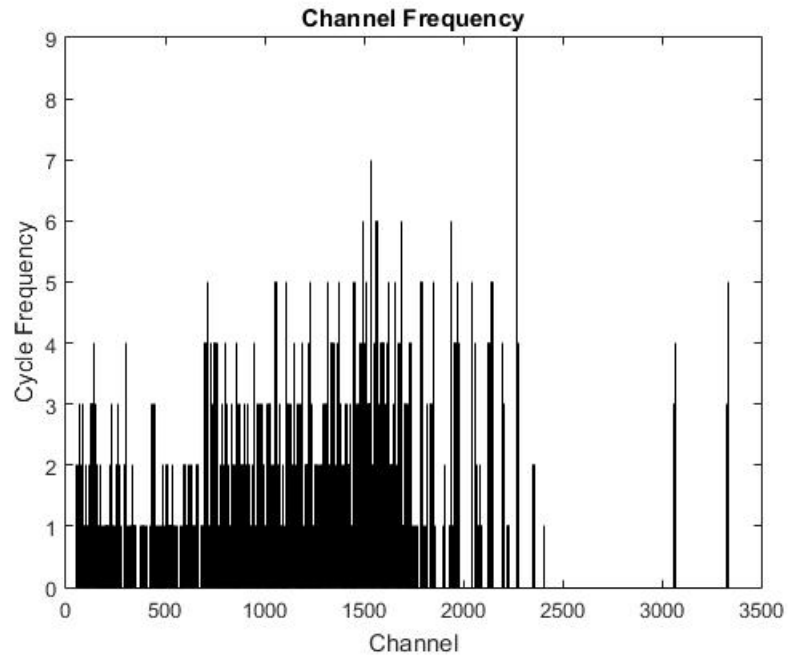


Figure 27: The 95% $\Delta\rho_{s,HEU,P_u}$ quantile for Template 3 displaying channel frequency among cycles.

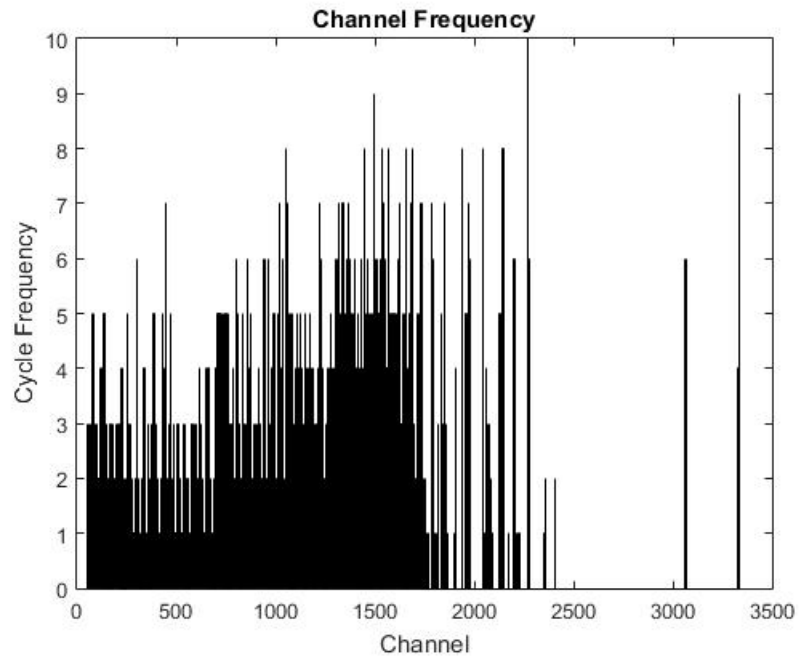


Figure 28: The 90% $\Delta\rho_{s,HEU,P_u}$ quantile for Template 3 displaying channel frequency among cycles.

Tables 21 and 22 show the number of channels seen in at least 30 % of the cycles for the 98th and 95th percentiles. Template 3 identified fewer channels than Templates 1 and 2. Further, the channels identified were not as consistently seen among the twenty cycles. Only one channel was seen in at least 45 % of the cycles for the 95th and only one channel was seen in at least 50 % of the cycles for the 90th percentile; a much lower consistency than the minimum of 80 % seen for Templates 1 and 2.

Channel	Frequency	Percentage
1565	6	30
1939	6	30

Table 21: Channels present in at least 30% of the cycles for the 98th percentile for Template 3.

Channel	Frequency	Percentage
1497	6	30
1535	7	35
1565	6	30
1687	6	30
1939	6	30
2273	9	45

Table 22: Channels present in at least 30% of the cycles for the 95th percentile for Template 3.

Table 23 shows the channels identified in each of the twenty cycles at each percentile for Template 4. The 98th percentile returned 36 channels on average, while the 95th and 90th percentiles returned 89 and 177 channels, respectively.

3.5.4 Template 4 $\Delta\rho_{s,HEU,Pu}$ Quantiles

		$\Delta\rho_{s,HEU,Pu}$ Percentile		
		0.90	0.95	0.98
Cycle	1	169	84	34
	2	170	88	39
	3	176	89	35
	4	177	89	36
	5	176	88	36
	6	187	90	39
	7	173	87	39
	8	176	89	35
	9	175	90	35
	10	170	85	34
	11	177	93	36
	12	174	92	36
	13	178	93	37
	14	179	88	38
	15	182	88	35
	16	182	87	37
	17	183	91	37
	18	182	88	35
	19	181	94	37
	20	176	88	37

Table 23: Total number of channels identified in each cycle for all three percentiles for Template 4.

Figures 29 through 31 show how the channels varied based on the $\Delta\rho_{s,HEU,Pu}$ percentile. Template 4, like Template 3, was less consistent than Templates 1 and 2. More channels were identified at the lower percentiles; however, only two channels were identified in at least 50 % of the cycles for the 90th percentile. Therefore, channels present in at least 30 % of cycles were included for evaluation.

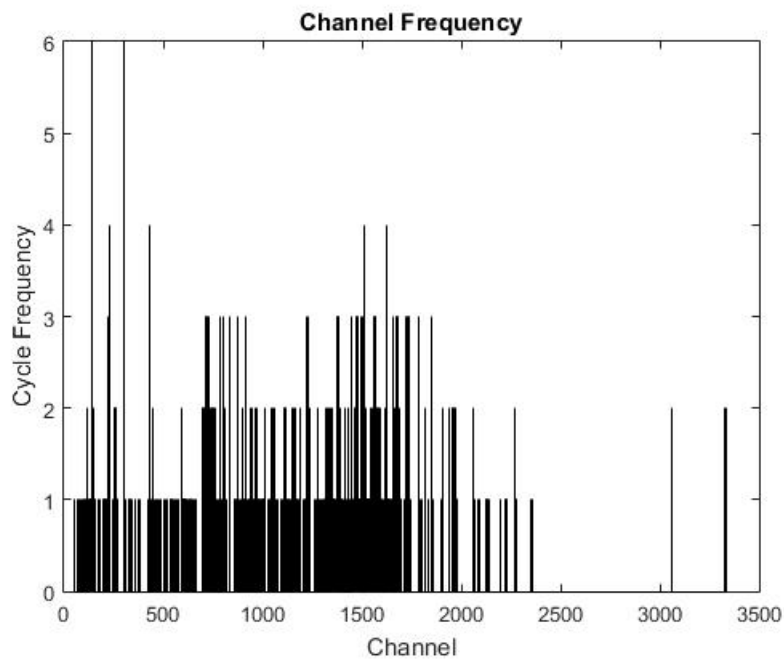


Figure 29: The 98% $\Delta\rho_{s,HEU,Pu}$ quantile for Template 4 displaying channel frequency among cycles.

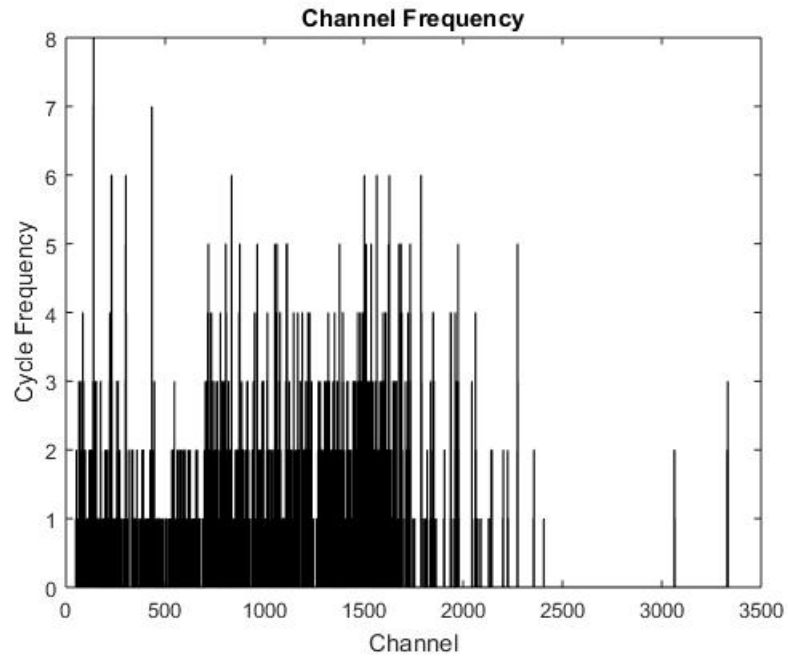


Figure 30: The 95% $\Delta\rho_{s,HEU,P_u}$ quantile for Template 4 displaying channel frequency among cycles.

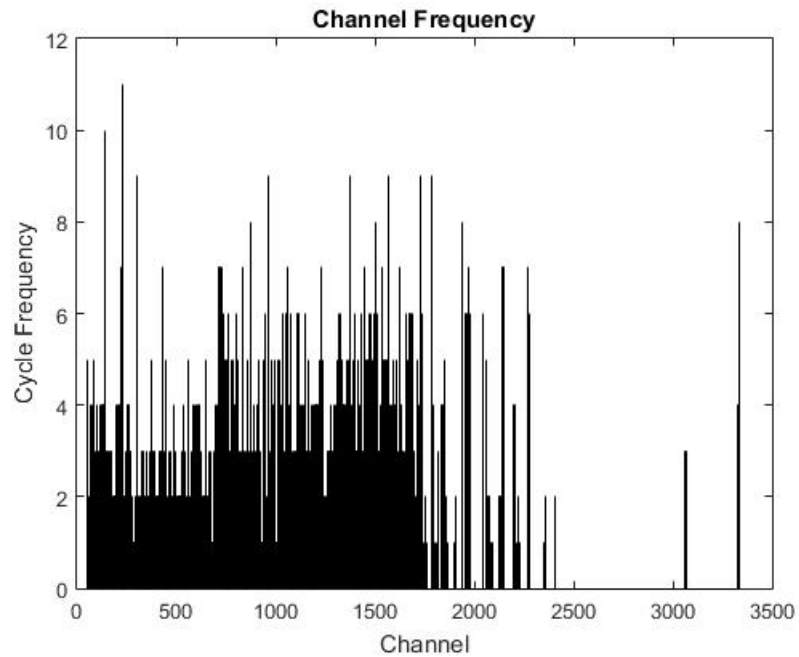


Figure 31: The 90% $\Delta\rho_{s,HEU,P_u}$ quantile for Template 4 displaying channel frequency among cycles.

Channel	Frequency	Percentage
140	6	30
302	6	30

Table 24: Channels present in at least 30% of the cycles for the 98th percentile for Template 4.

Channel	Frequency	Percentage
139	7	35
140	8	40
230	6	30
231	6	30
302	6	30
433	7	35
834	6	30
1503	6	30
1628	6	30
1787	6	30

Table 25: Channels present in at least 30% of the cycles for the 95th percentile for Template 4.

Tables 24 and 25 display the channels seen in 30 % of the cycles for the 98th and 95th percentiles, respectively. In the 98th percentile, the only two channels identified in at least 30 % of the cycles were Channel 140 and Channel 302. The 95th percentile returned several more channels; however, many of these channels were identified by other templates with more consistency.

In summary, it was observed that the 98th percentile provided too little of

data at 36 channels on average, resulting in less channels being identified with enough consistency. The 95th percentile resulted in 89 channels on average resulting in more channels being identified with consistency across the twenty cycles. The benefit of using the 90th percentile appeared minimal.

Table 26 summarizes the channels identified in the 95th percentile. The percent frequency for each of the four templates is listed. For every channel except Channel 231, one of the four template patterns identified the channel as being significant. However, it was observed based on the percentage of channel frequency that some templates were a better fit than others. Overall, Templates 3 and 4 identified channels less consistently across the twenty cycles. Templates 1 and 2 identified the channels used for the proof-of-concept of this research.

Channel	Template 1	Template 2	Template 3	Template 4
139	100	100	20	35
140	90	90	5	40
230	90	90	10	30
231	55	55	NA	30
301	100	100	5	25
302	100	100	10	30
433	75	75	10	35
834	70	70	15	30
964	85	85	10	25
965	90	90	5	10
1497	20	20	30	15
1503	20	20	15	30
1535	5	5	35	15
1565	20	20	30	30
1628	15	15	25	30
1687	15	15	30	25
1787	15	15	20	30
1939	20	20	30	20
2273	30	30	45	25

Table 26: Percentage of channel frequency for all four templates.

3.6 Cycle Consistency

For the 98th percentile, Templates 1 and 2 identified six channels that occurred in at least 80 % of the cycles. As mentioned previously, Templates 3 and 4

did not maintain the consistency seen for Templates 1 and 2; therefore, channels that were seen in at least 30 % of cycles were included as significant. Templates 3 and 4 identified two channels for the 98th percentile. Using the 95th $\Delta\rho_{s,HEU,Pu}$ percentile, Templates 1 and 2 identified nine channels that occurred in at least 80 % of cycles. Templates 3 and 4 identified six and ten channels, respectively, that showed up in at least 30 % of cycles. The 95th percentile was chosen as it provided enough channels for the proof-of-concept for this research.

3.7 Identifying Significant Channels

In the previous sections, discussion consisted of how the $\Delta\rho_{s,HEU,Pu}$ quantile was used as a clustering technique to identify channels that may be significant and how the various $\Delta\rho_{s,HEU,Pu}$ percentiles effected how consistently channels were seen in the twenty cycles. While using the 95th percentile increased the overall number of channels identified and increased the consistency of channels previously identified, the $\Delta\rho_{s,HEU,Pu}$ threshold used was lowered. For the 98th percentile the $\Delta\rho_{s,HEU,Pu}$ threshold ranged from 0.79-0.92 while the $\Delta\rho_{s,HEU,Pu}$ threshold range for the 95th percentile was 0.59-0.76. This led to the inclusion of channels with a wide range of $\Delta\rho_{s,HEU,Pu}$ values across cycles and channels making it difficult to determine if a channel was significant based on the $\Delta\rho_{s,HEU,Pu}$ value alone. In order to ensure only channels with the greatest significance were evaluated, the relationship between the individual ρ_s and the $\Delta\rho_{s,HEU,Pu}$ values required further investigation.

3.7.1 Template 1 $\Delta\rho_{s,HEU,Pu}$ and ρ_s

Lattice, a graphics package in R, was used to plot the channels identified as significant for both the 98th and 95th percentiles. In line with the characteristic behavior of radioactive decay, the temporal behavior for each channel varied from cycle to cycle; therefore, plots for each cycle were generated. Some cycles appeared to show greater differences between uranium and plutonium for the same channel. To explore these variations, the individual ρ_s and $\Delta\rho_{s,HEU,Pu}$ values for each of the twenty cycles for each channel were evaluated. Spreadsheets were created in Excel for both the 98th and 95th percentiles.

It was found that the relationship between the individual ρ_s and the $\Delta\rho_{s,HEU,Pu}$ values was important. Below a $\Delta\rho_{s,HEU,Pu}$ value of 1, the signs of the individual ρ_s values could potentially be the same, indicating that the association trends were either both positive or both negative. When the signs of the individual ρ_s values were the same, the difference in temporal behavior between the materials was minimal. When the signs of the individual ρ_s were opposite one another below a $\Delta\rho_{s,HEU,Pu}$ value of 1, significant differences between the materials was seen. Implementing a $\Delta\rho_{s,HEU,Pu}$ threshold value of 1 was considered; however, this would have eliminated some cycles that showed significant differences between the two materials and would have greatly limited the channel consistency across cycles. The 95th percentile included channels with at least a $\Delta\rho_{s,HEU,Pu}$ threshold value of 0.70 and provided enough channels to evaluate for the proof-of-concept of this research. However, values below

0.70 may be useful for identifying additional significant channels but would require further evaluation and rules would need to be discovered through the implementation of additional machine learning techniques. Further evaluation of values below 0.70 should be considered for future work. Based on these findings, the data was clustered by the $\Delta\rho_{s,HEU,Pu}$ value and then further clustered by identifying cycles where the individual ρ_s values had different signs. This resulted in a set of channels that displayed the greatest differences consistently across the twenty cycles between uranium and plutonium.

Tables 27 through 29 show the final channels identified as significant for each template and their per cent frequency among the twenty cycles. Three channels (231, 433 and 834) were identified more consistently by Templates 1 and 2 ; however, they were present in less than 80 % of the cycles. These channels were evaluated under Template 4 since they were identified in at least 30 % of the cycles for that template. To visualize the temporal behavior in each channel for both uranium and plutonium, plots were generated in R and are shown in the next section.

Channel	Percentage
139	100
140	90
230	85
301	95
302	95
964	85
965	90

Table 27: Channels identified by Templates 1 and 2.

As seen in Table 27, by eliminating cycles where the individual ρ_s had the same sign, a reduction in cycle consistency was seen for channels 230, 301, and 302 identified by Templates 1 and 2. Further, Channel 874 and Channel 231 were eliminated, resulting in the identification of seven channels as significant.

Channel	Percentage
1535	35
1565	30
1687	30
1939	30
2273	45

Table 28: Channels identified by Template 3.

As seen in Table 28, eliminating cycles where the individual ρ_s had the same sign led to the elimination of Channel 1497, originally identified by Template 3 as

being present in 30 % of the cycles.

Channel	Percentage
231	30
433	35
834	30
1503	30
1628	30
1787	30

Table 29: Channels identified by Template 4.

Similarly, as seen in Table 29, eliminating cycles where the individual ρ_s had the same sign led to the elimination of four channels (139, 140, 230, and 302) originally identified by Template 4 as being present in 30 % of the cycles.

3.8 Significant Channels

The next sections will display the temporal behavior seen in each of the identified channels based on which template had the best fit. Overall, eighteen channels were identified as showing significant differences between materials. Channels that were identified in less than 80 % of the cycles but more than 30 % will be displayed under Templates 3 and 4. Templates 1 and 2 had the same numerical ρ_s values; however, since Template 2 is the inverse of Template 1, their ρ_s values had opposite signs. For simplicity, only the ρ_s values for Template 1 are given below for each plot

of temporal behavior for Template 1.

3.8.1 Template 1 Channel 139

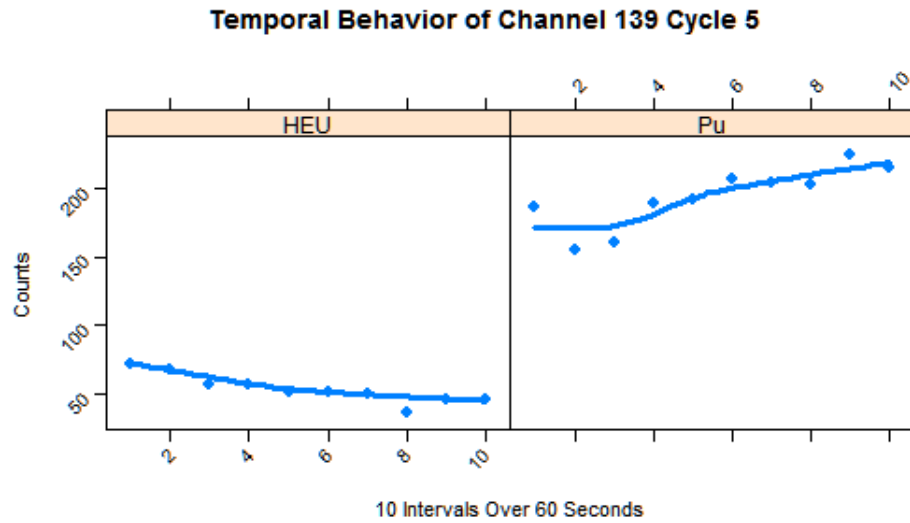


Figure 32: Channel 139 Cycle 5 has a $\rho_{s,HEU}$ of 0.95, a $\rho_{s,Pu}$ of -0.90 and a $\Delta\rho_{s,HEU,Pu}$ of 1.85.

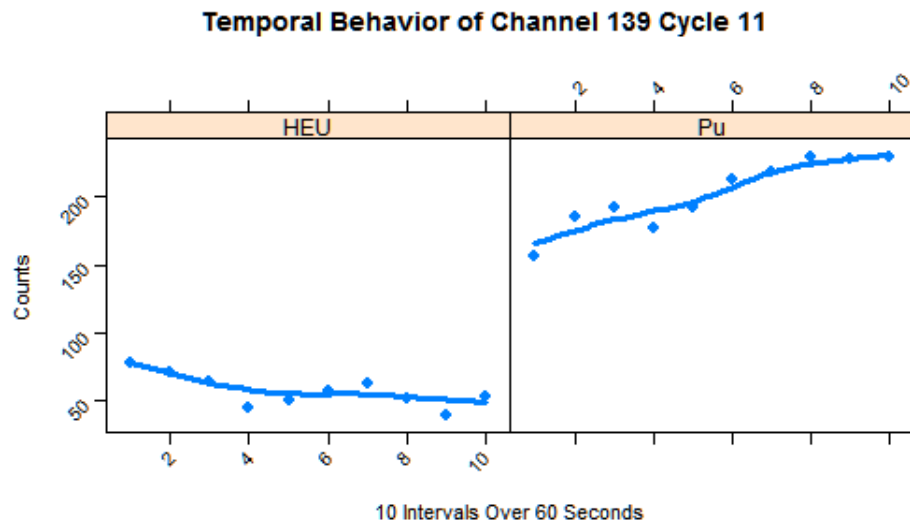


Figure 33: Channel 139 Cycle 11 has a $\rho_{s,HEU}$ of 0.62, a $\rho_{s,Pu}$ of -0.91 and a $\Delta\rho_{s,HEU,Pu}$ of 1.53.

3.8.2 Template 1 Channel 140

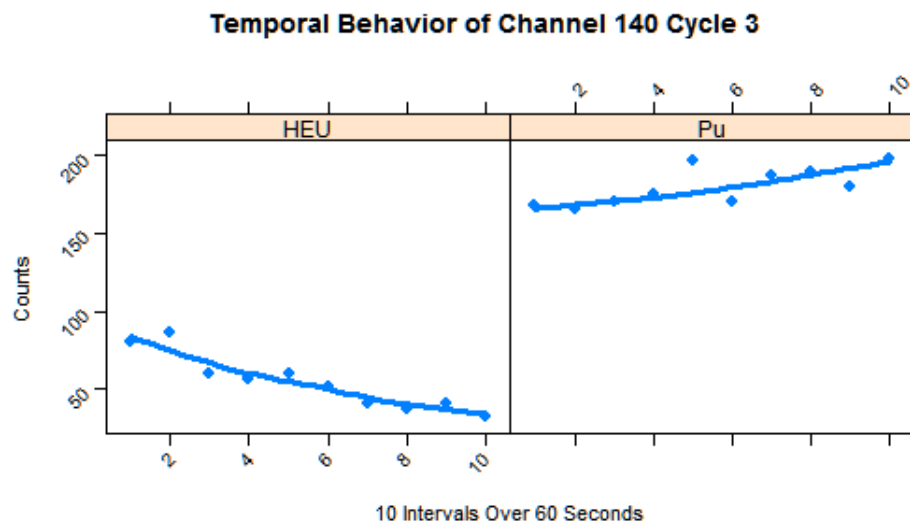


Figure 34: Channel 140 Cycle 3 has a $\rho_{s,HEU}$ of 0.94, a $\rho_{s,Pu}$ of -0.79 and a $\Delta\rho_{s,HEU,Pu}$ of 1.73.

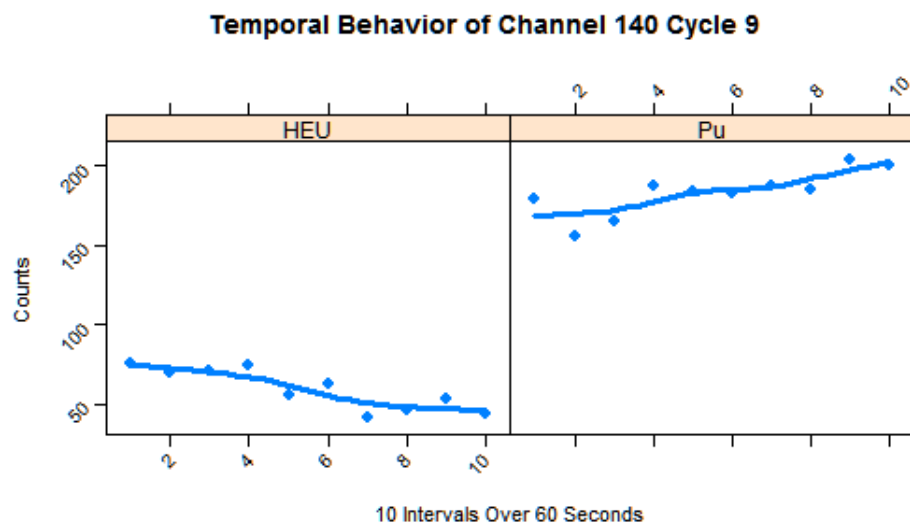


Figure 35: Channel 140 Cycle 9 has a $\rho_{s,HEU}$ of 0.85, a $\rho_{s,Pu}$ of -0.82 and a $\Delta\rho_{s,HEU,Pu}$ of 1.67.

3.8.3 Template 1 Channel 230

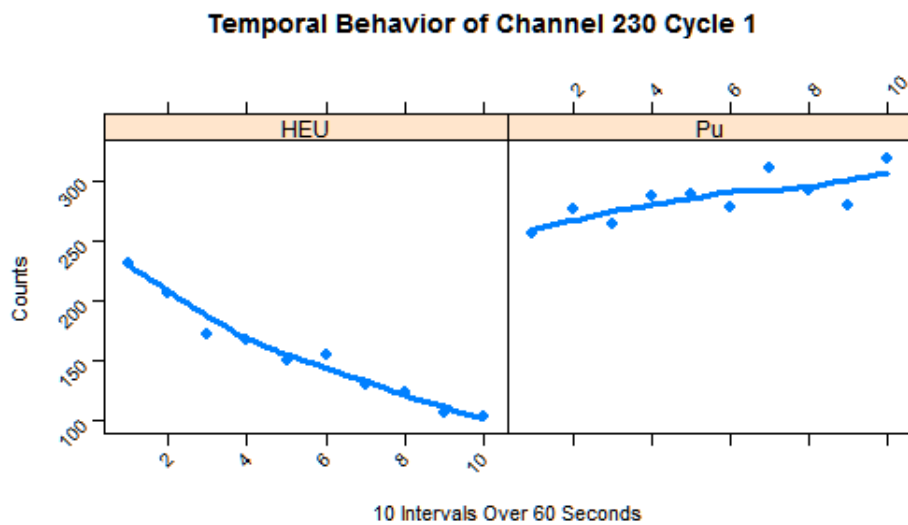


Figure 36: Channel 230 Cycle 1 has a $\rho_{s,HEU}$ of 0.98, a $\rho_{s,Pu}$ of -0.79 and a $\Delta\rho_{s,HEU,Pu}$ of 1.77.

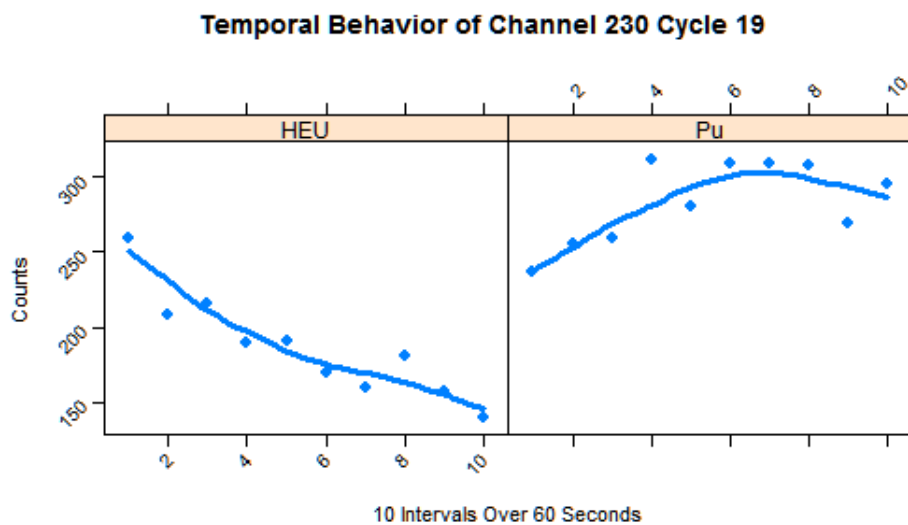


Figure 37: Channel 230 Cycle 19 has a $\rho_{s,HEU}$ of 0.93, a $\rho_{s,Pu}$ of -0.47 and a $\Delta\rho_{s,HEU,Pu}$ of 1.40.

3.8.4 Template 1 Channel 301

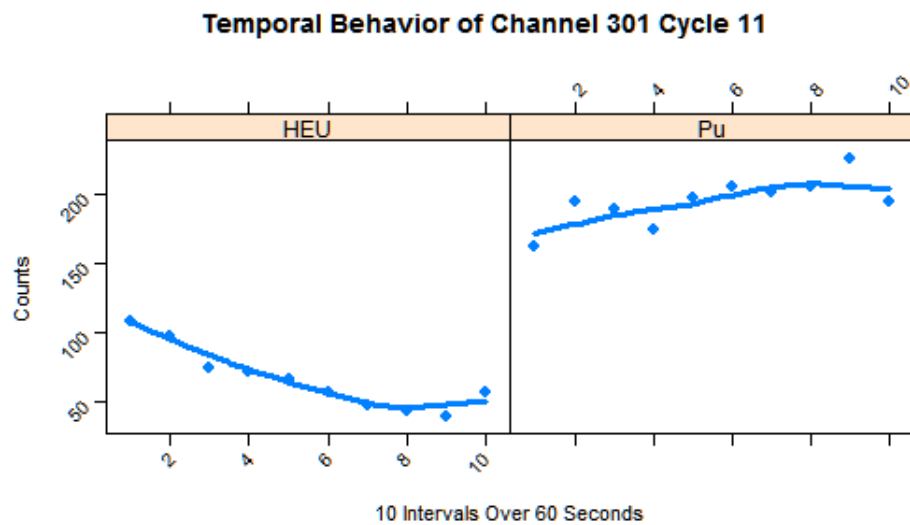


Figure 38: Channel 301 Cycle 11 has a $\rho_{s,HEU}$ of 0.90, a $\rho_{s,Pu}$ of -0.71 and a $\Delta\rho_{s,HEU,Pu}$ of 1.61.

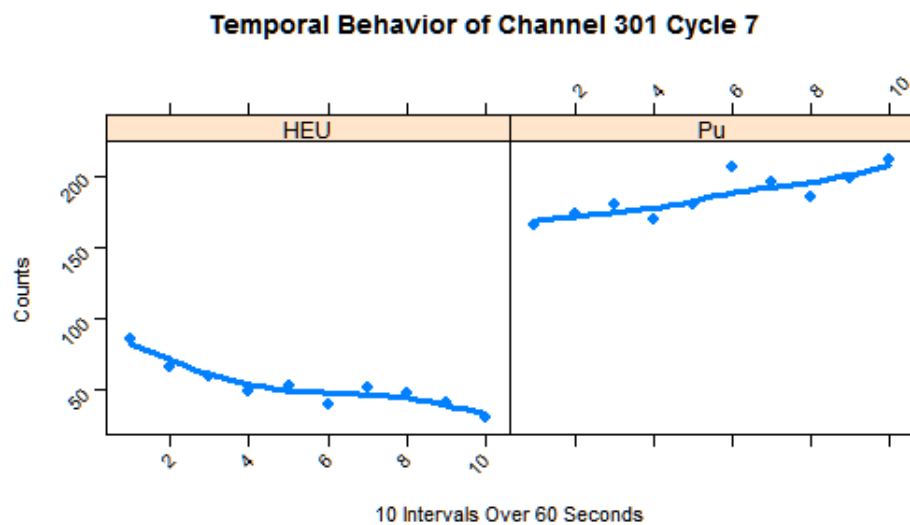


Figure 39: Channel 301 Cycle 7 has a $\rho_{s,HEU}$ of 0.87, a $\rho_{s,Pu}$ of -0.86 and a $\Delta\rho_{s,HEU,Pu}$ of 1.73.

3.8.5 Template 1 Channel 302

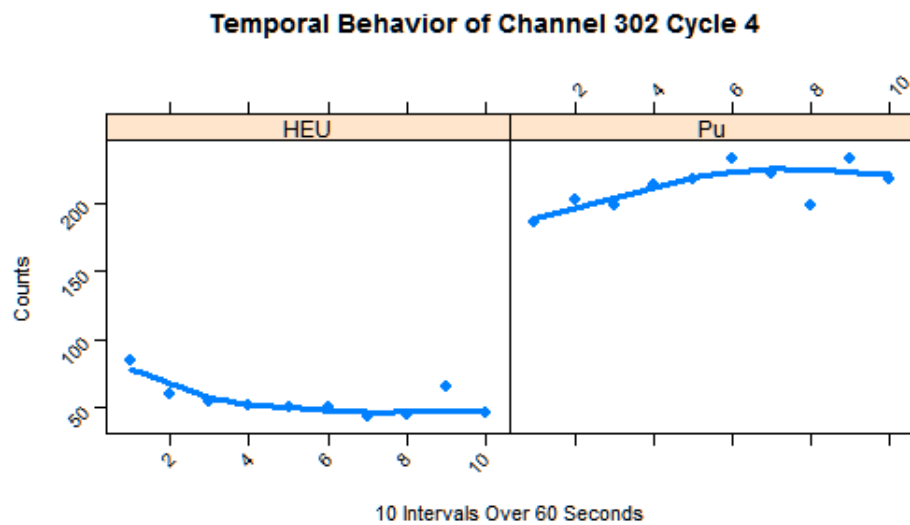


Figure 40: Channel 302 Cycle 4 has a $\rho_{s,HEU}$ of 0.58, a $\rho_{s,Pu}$ of -0.58 and a $\Delta\rho_{s,HEU,Pu}$ of 1.16.

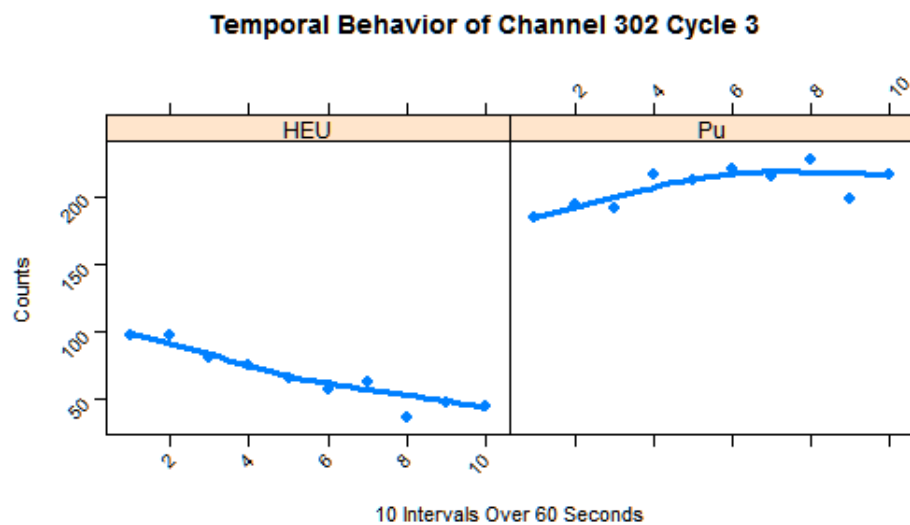


Figure 41: Channel 302 Cycle 3 has a $\rho_{s,HEU}$ of 0.93, a $\rho_{s,Pu}$ of -0.63 and a $\Delta\rho_{s,HEU,Pu}$ of 1.56.

3.8.6 Template 1 Channel 964

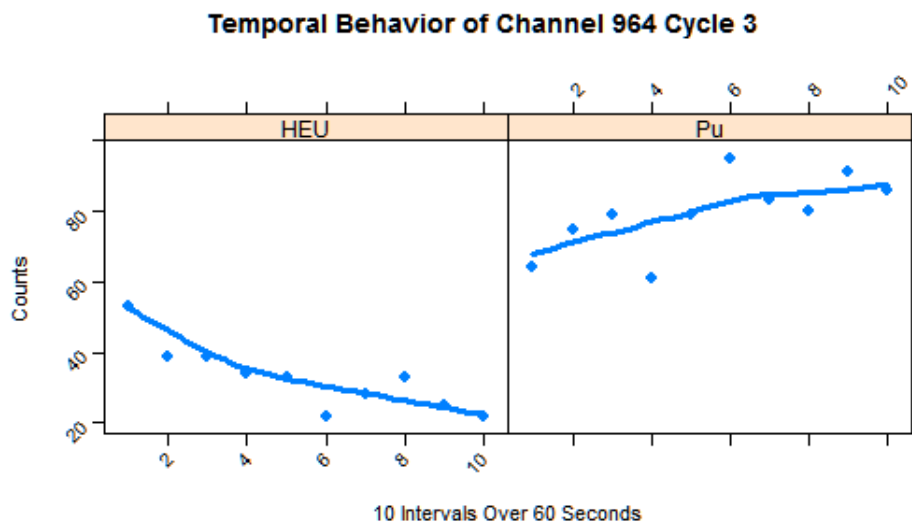


Figure 42: Channel 964 Cycle 3 has a $\rho_{s,HEU}$ 0.87, a $\rho_{s,Pu}$ of -0.77 and a $\Delta\rho_{s,HEU,Pu}$ of 1.64.

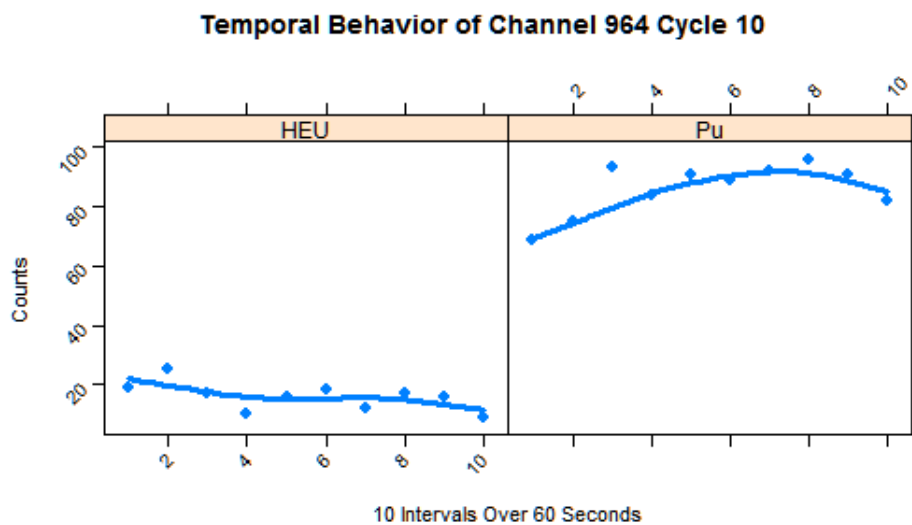


Figure 43: Channel 964 Cycle 10 has a $\rho_{s,HEU}$ of 0.63, a $\rho_{s,Pu}$ of -0.39 and a $\Delta\rho_{s,HEU,Pu}$ of 1.02.

3.8.7 Template 1 Channel 965

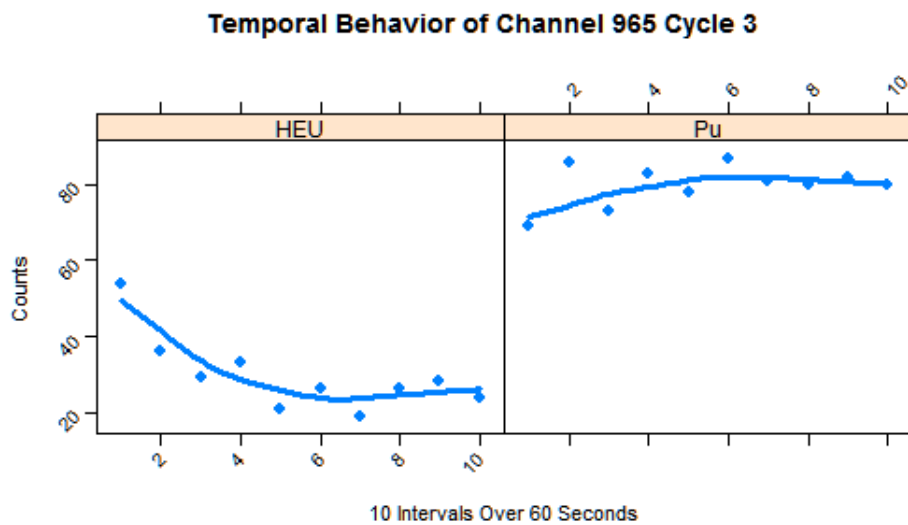


Figure 44: Channel 965 Cycle 3 has a $\rho_{s,HEU}$ of 0.69, a $\rho_{s,Pu}$ of -0.18 and a $\Delta\rho_{s,HEU,Pu}$ of 0.87.

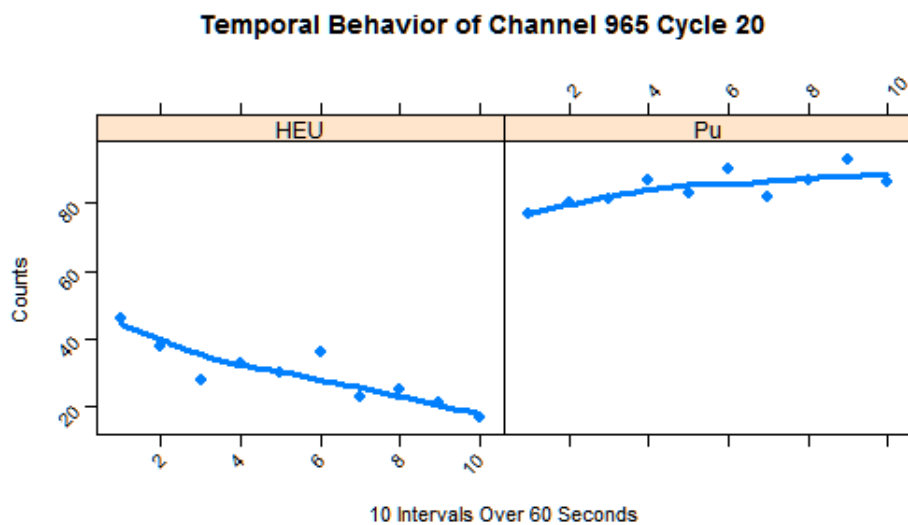


Figure 45: Channel 965 Cycle 20 has a $\rho_{s,HEU}$ of 0.87, a $\rho_{s,Pu}$ of -0.71 and a $\Delta\rho_{s,HEU,Pu}$ of 1.58.

The channels identified by Templates 1 and 2 all displayed significant differences in temporal behavior between the two materials. Given their cycle consistency, and significant attributes, these channels could be used as a model for the identification of an unknown sample of SNM.

3.8.8 Template 3 Channel 1535

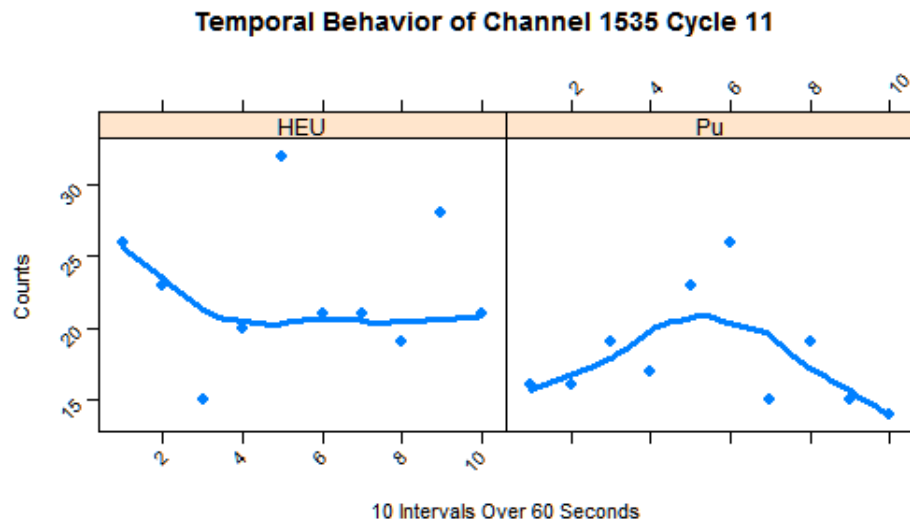


Figure 46: Channel 1535 Cycle 11 has a $\rho_{s,HEU}$ of -0.34, a $\rho_{s,Pu}$ of 0.61 and a $\Delta\rho_{s,HEU,Pu}$ of 0.95.

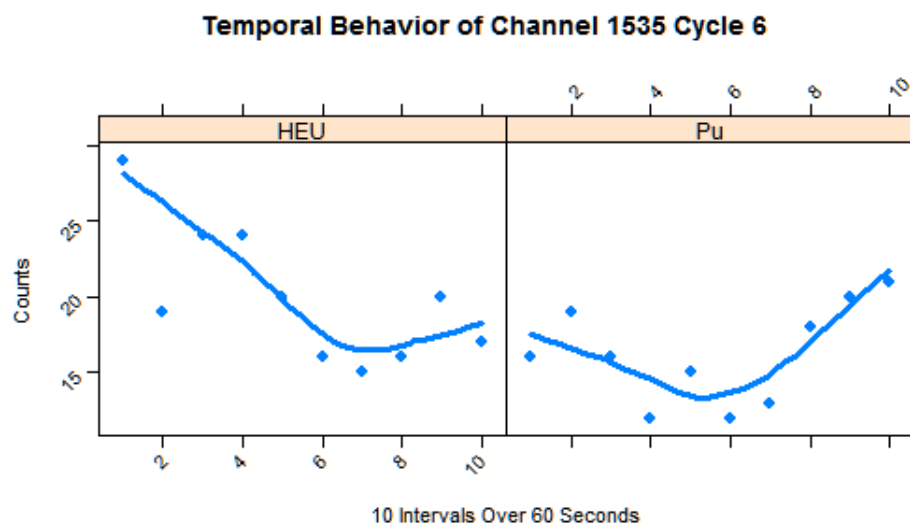


Figure 47: Channel 1535 Cycle 6 has a $\rho_{s,HEU}$ of 0.13, a $\rho_{s,Pu}$ of -0.63 and a $\Delta\rho_{s,HEU,Pu}$ of 0.76.

3.8.9 Template 3 Channel 1687

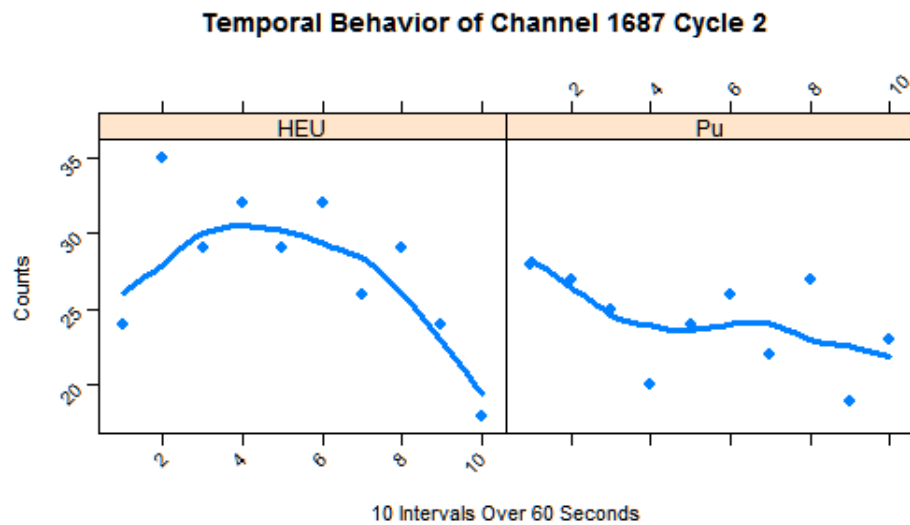


Figure 48: Channel 1687 Cycle 2 has a $\rho_{s,HEU}$ of 0.74, a $\rho_{s,Pu}$ of -0.22 and a $\Delta\rho_{s,HEU,Pu}$ of 0.96.

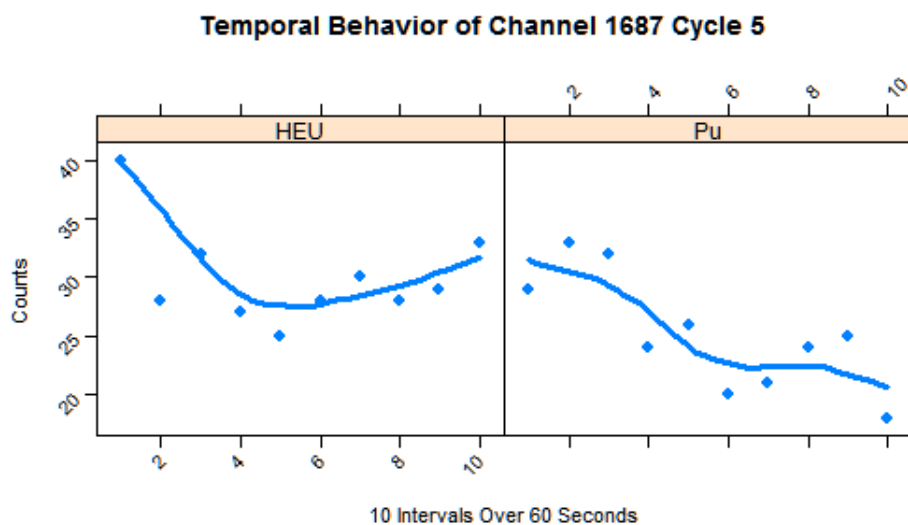


Figure 49: Channel 1687 Cycle 5 has a $\rho_{s,HEU}$ of -0.65, a $\rho_{s,Pu}$ of 0.17 and a $\Delta\rho_{s,HEU,Pu}$ of 0.82.

3.8.10 Template 3 Channel 1939

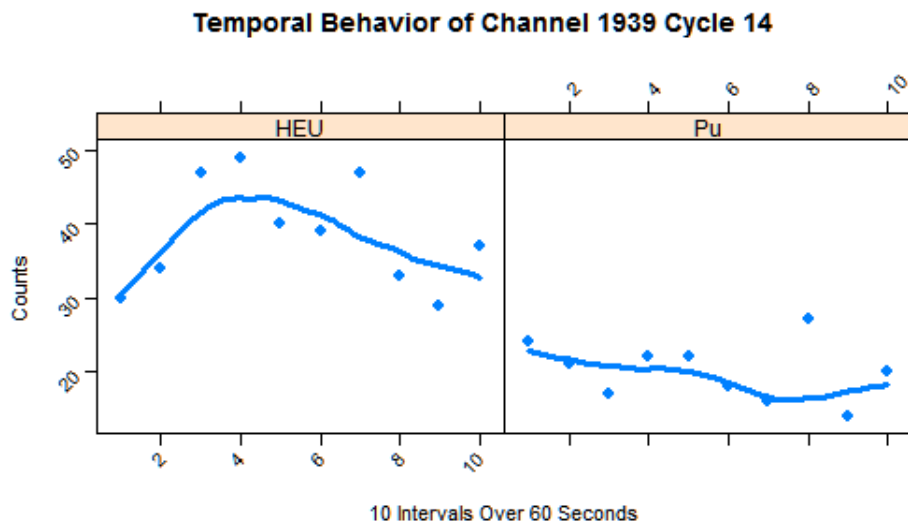


Figure 50: Channel 1939 Cycle 14 has a $\rho_{s,HEU}$ of 0.79, a $\rho_{s,Pu}$ of -0.05 and a $\Delta\rho_{s,HEU,Pu}$ of 0.84.

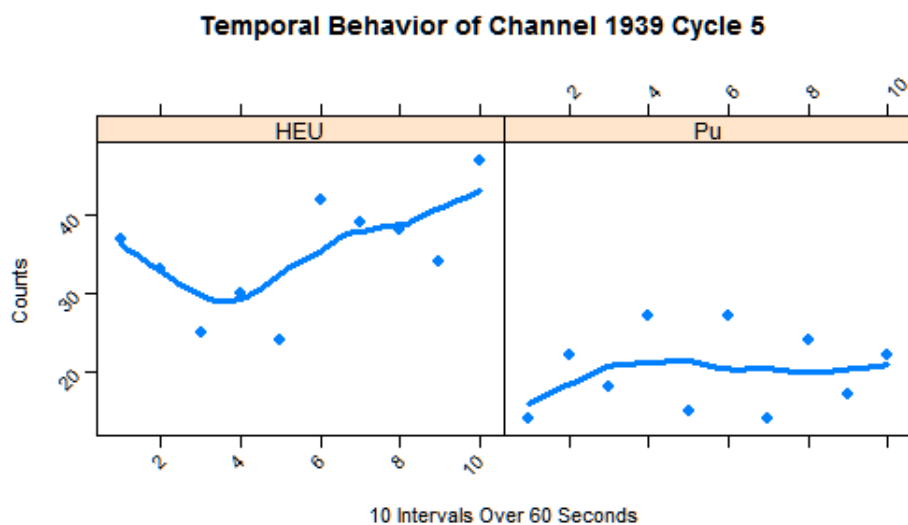


Figure 51: Channel 1939 Cycle 5 has a $\rho_{s,HEU}$ of -0.61, a $\rho_{s,Pu}$ of 0.40 and a $\Delta\rho_{s,HEU,Pu}$ of 1.01.

3.8.11 Template 3 Channel 2273

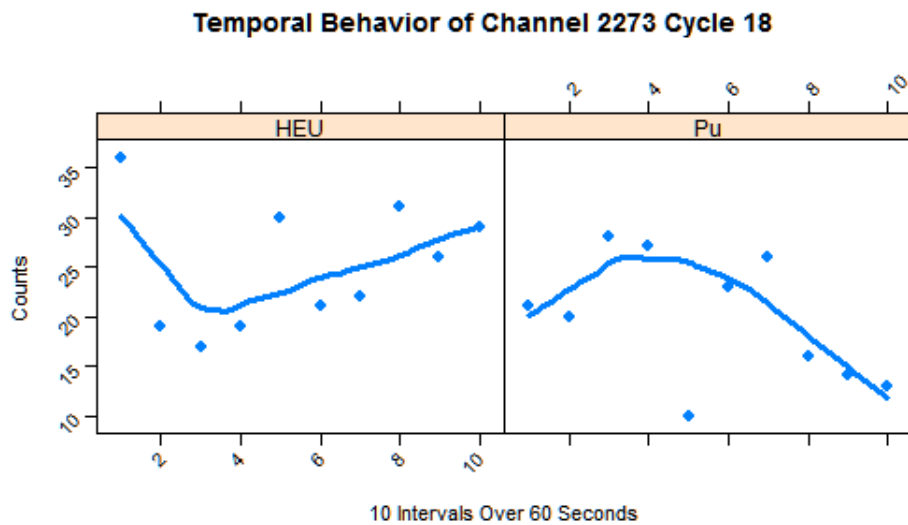


Figure 52: Channel 2273 Cycle 18 has a $\rho_{s,HEU}$ of -0.71, a $\rho_{s,Pu}$ of 0.47 and a $\Delta\rho_{s,HEU,Pu}$ of 1.18.

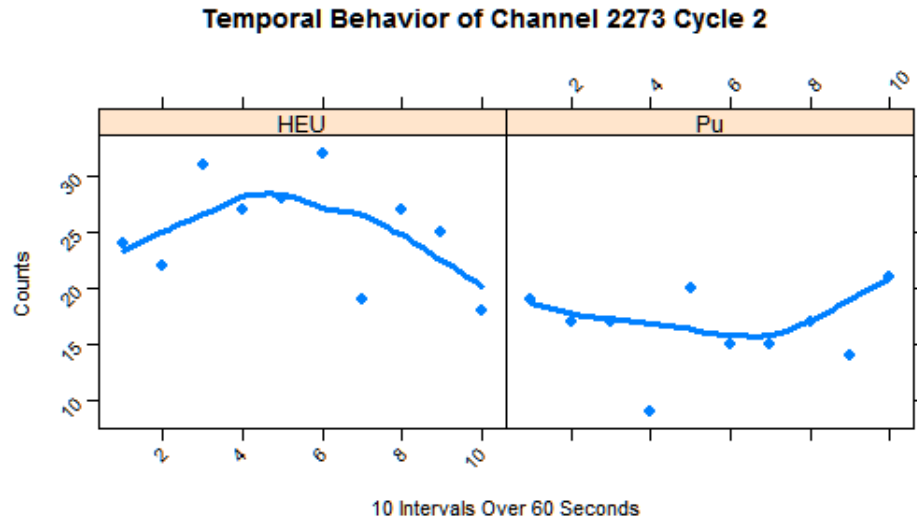


Figure 53: Channel 2273 Cycle 2 has a $\rho_{s,HEU}$ of 0.63, a $\rho_{s,Pu}$ of -0.37 and a $\Delta\rho_{s,HEU,Pu}$ of 1.00.

While Template 3 identified channels that displayed differences in temporal behavior between the two materials, the channels were not as consistent among the cycles as the channels identified by Templates 1 and 2. However, channels identified for Template 3 were included for completeness. Further evaluation of Template 3 should be considered for future work, as Template 3 may be able to identify channels with more consistency if certain parameters such as count time were changed.

3.8.12 Template 4 Channel 231

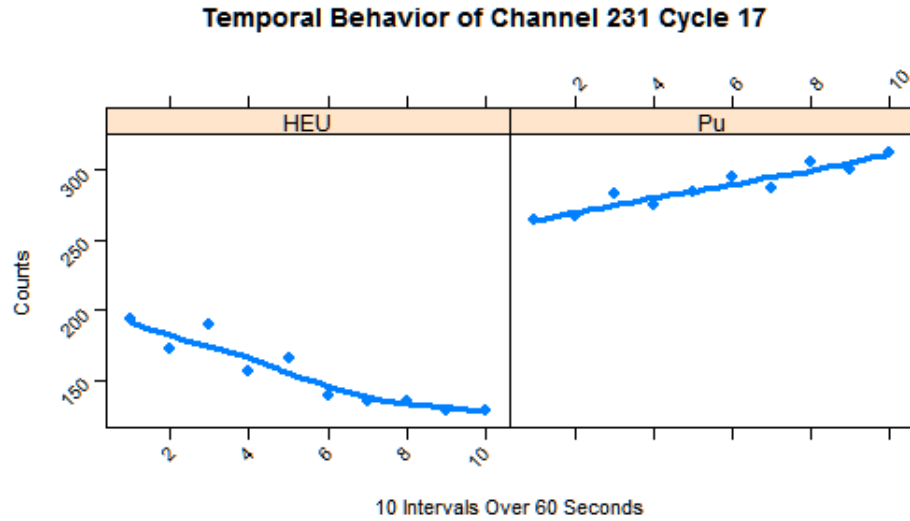


Figure 54: Channel 231 Cycle 17 has a $\rho_{s,HEU}$ of -0.59, a $\rho_{s,Pu}$ of 0.55 and a $\Delta\rho_{s,HEU,Pu}$ of 1.14.

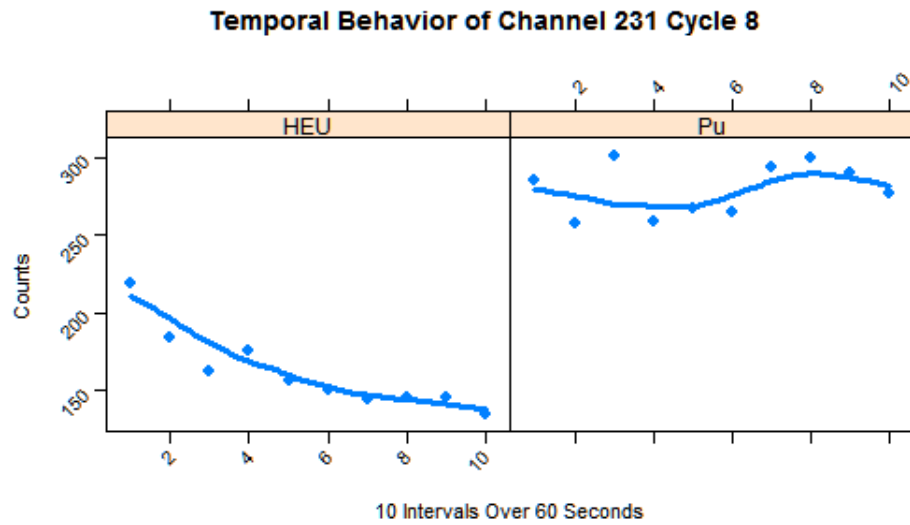


Figure 55: Channel 231 Cycle 8 has a $\rho_{s,HEU}$ of -0.52, a $\rho_{s,Pu}$ of 0.33 and a $\Delta\rho_{s,HEU,Pu}$ of 0.85.

Channel 231 was one of the channels identified by Templates 1 and 2 more consistently but in less than 80 % of the cycles. The temporal behavior was more representative of decay for HEU. The $\rho_{s,HEU}$ value for Cycle 8, Template 1 was 0.94 and for Cycle 17, Template 1 the $\rho_{s,HEU}$ value was 0.96 while the $\rho_{s,Pu}$ value was -0.96. Channel 231 shows strong differences between uranium and plutonium in several cycles, it does not show up consistently across all cycles for any of the templates.

3.8.13 Template 4 Channel 433

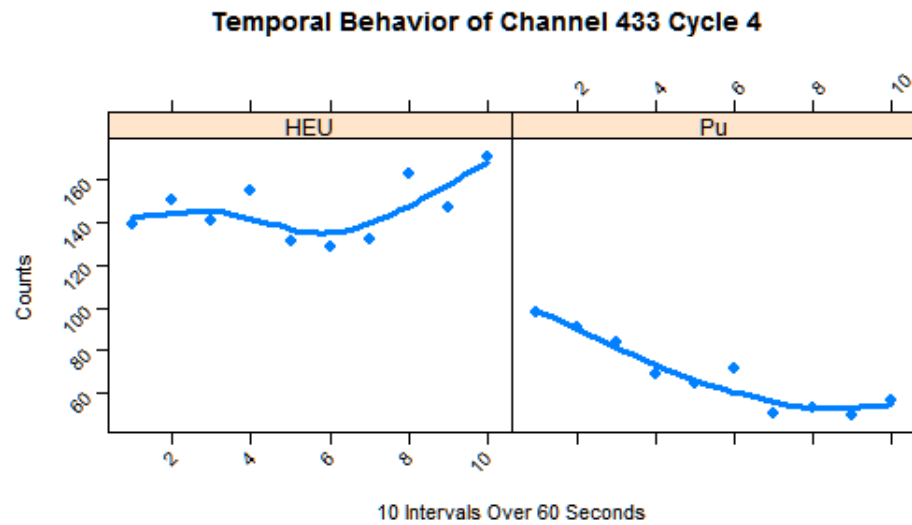


Figure 56: Channel 433 Cycle 4 has a $\rho_{s,HEU}$ of 0.50, a $\rho_{s,Pu}$ of -0.40 and a $\Delta\rho_{s,HEU,Pu}$ of 0.90.

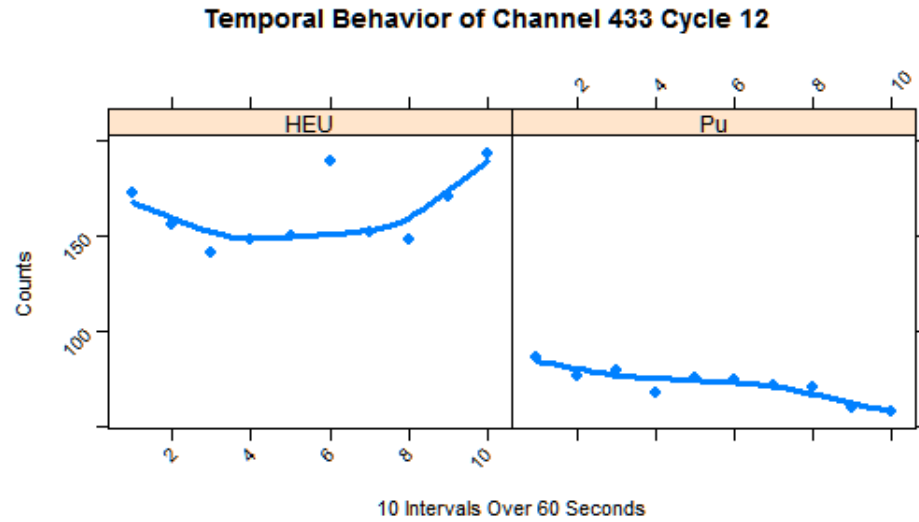


Figure 57: Channel 433 Cycle 12 has a $\rho_{s,HEU}$ of 0.54, a $\rho_{s,Pu}$ of -0.46 and a $\Delta\rho_{s,HEU,Pu}$ of 1.00.

Channel 433 was another channel that was identified by Templates 1 and 2 with more consistency. The $\rho_{s,Pu}$ value for Cycle 4, Template 1 was 0.87 while the $\rho_{s,Pu}$ value for Cycle 12, Template 1 was 0.86. Like Channel 231, Channel 433 was not identified consistently enough by any of the templates. Channel 834, seen next, was the last of the three channels to be identified with more consistency by Templates 1 and 2.

3.8.14 Template 4 Channel 834

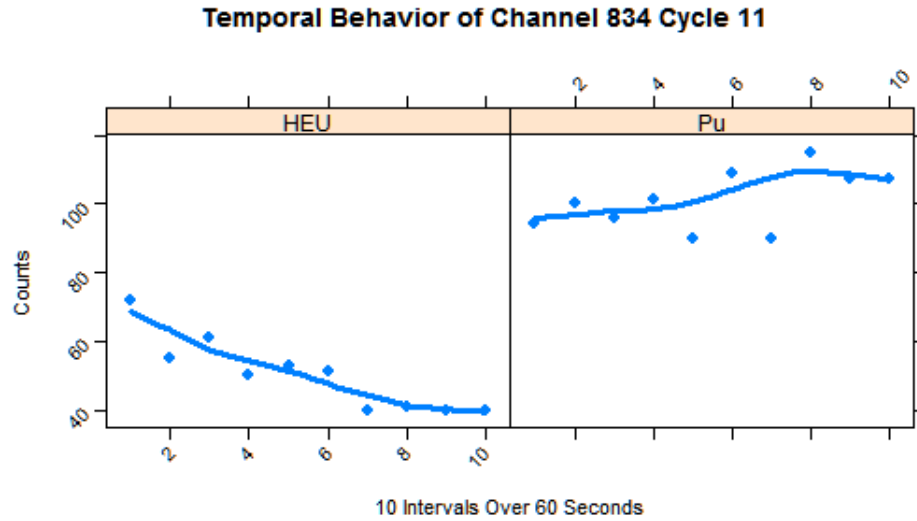


Figure 58: Channel 834 Cycle 11 has a $\rho_{s,HEU}$ of -0.52, a $\rho_{s,Pu}$ of 0.44 and a $\Delta\rho_{s,HEU,Pu}$ of 0.96.

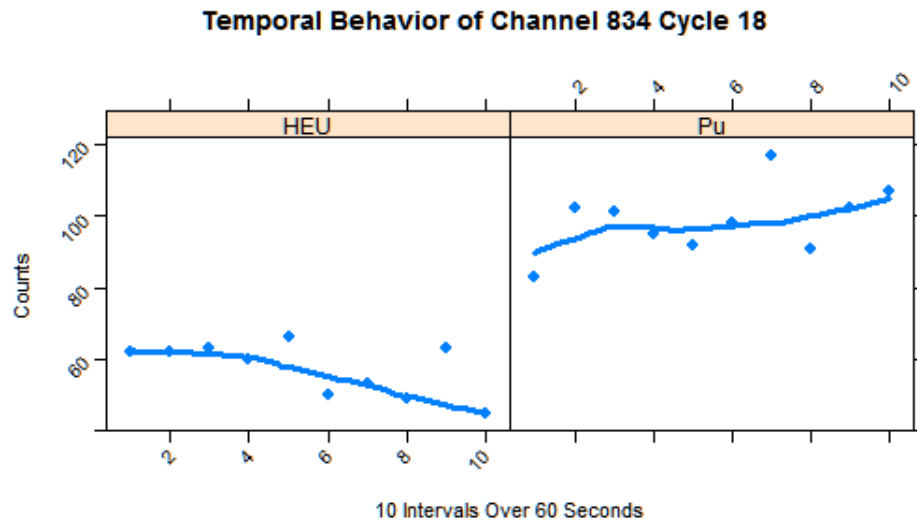


Figure 59: Channel 834 Cycle 18 has a $\rho_{s,HEU}$ of -0.49, a $\rho_{s,Pu}$ of 0.29 and a $\Delta\rho_{s,HEU,Pu}$ of 0.78.

3.8.15 Template 4 Channel 1503

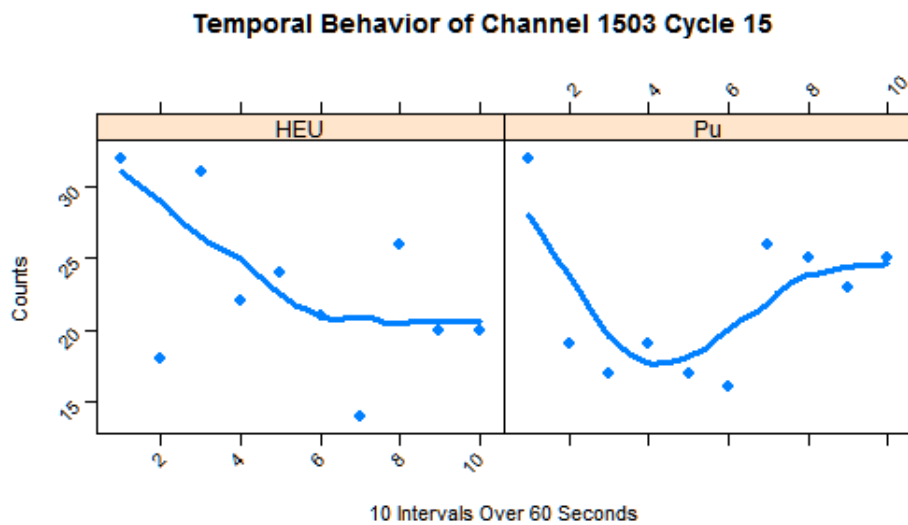


Figure 60: Channel 1503 Cycle 15 has a $\rho_{s,HEU}$ of -0.24, a $\rho_{s,Pu}$ of 0.68 and a $\Delta\rho_{s,HEU,Pu}$ of 0.92.

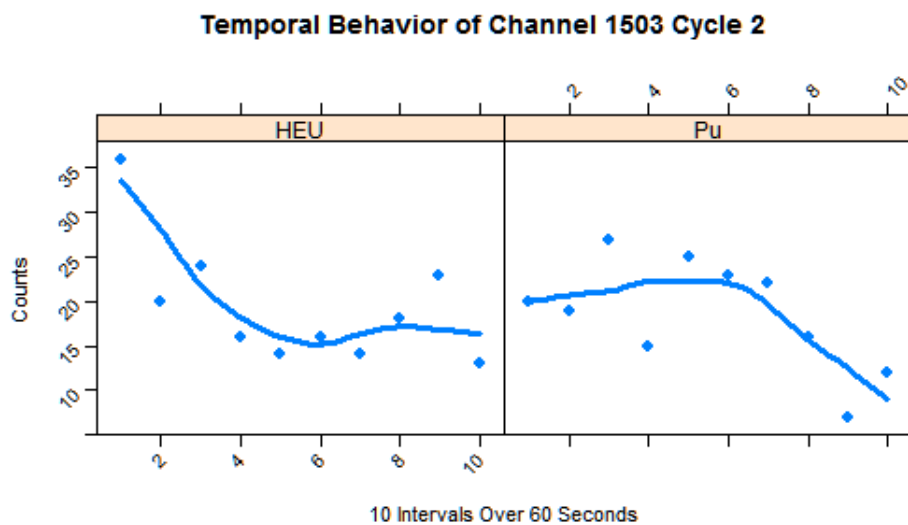


Figure 61: Channel 1503 Cycle 2 has a $\rho_{s,HEU}$ of 0.04, a $\rho_{s,Pu}$ of -0.67 and a $\Delta\rho_{s,HEU,Pu}$ of 0.71.

3.8.16 Template 4 Channel 1628

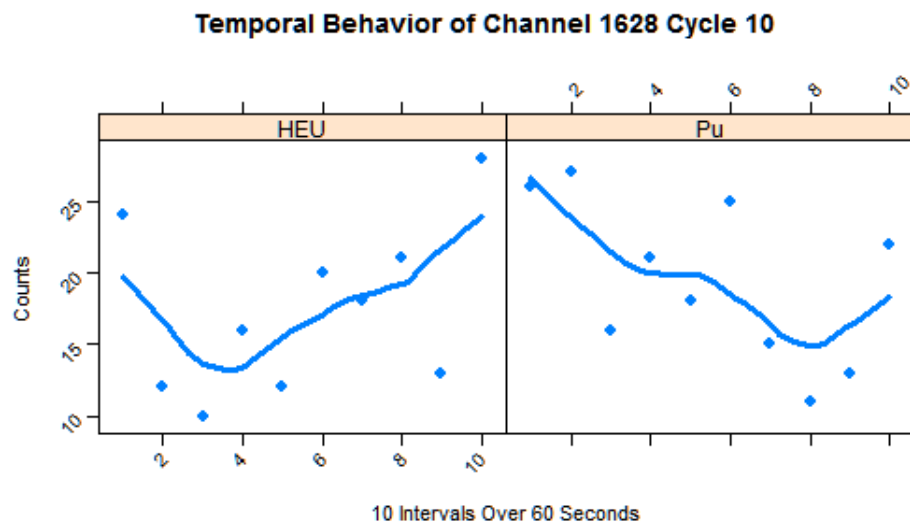


Figure 62: Channel 1628 Cycle 10 has a $\rho_{s,HEU}$ of 0.63, a $\rho_{s,Pu}$ of -0.17 and a $\Delta\rho_{s,HEU,Pu}$ of 0.80.

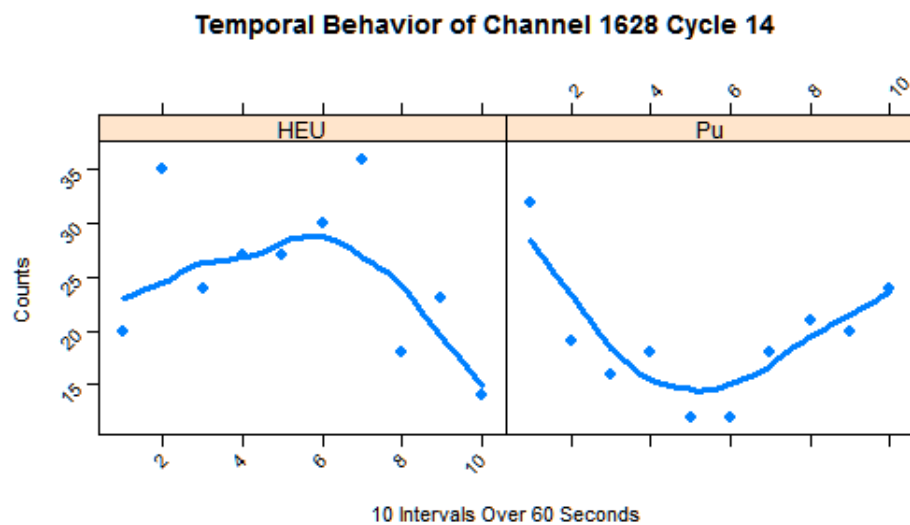


Figure 63: Channel 1628 Cycle 14 has a $\rho_{s,HEU}$ of -0.58, a $\rho_{s,Pu}$ of 0.81 and a $\Delta\rho_{s,HEU,Pu}$ of 1.39.

3.8.17 Template 4 Channel 1787

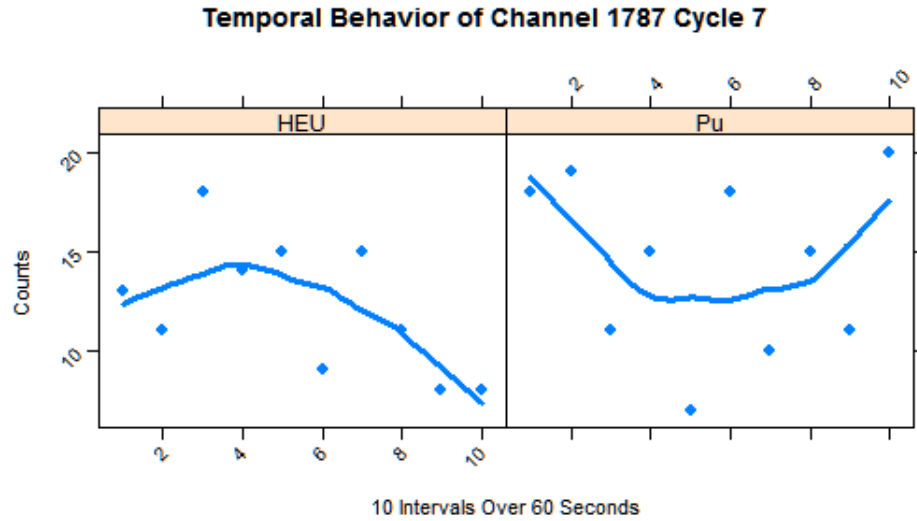


Figure 64: Channel 1787 Cycle 7 has a $\rho_{s,HEU}$ of -0.70, a $\rho_{s,Pu}$ of 0.42 and a $\Delta\rho_{s,HEU,Pu}$ of 1.12.

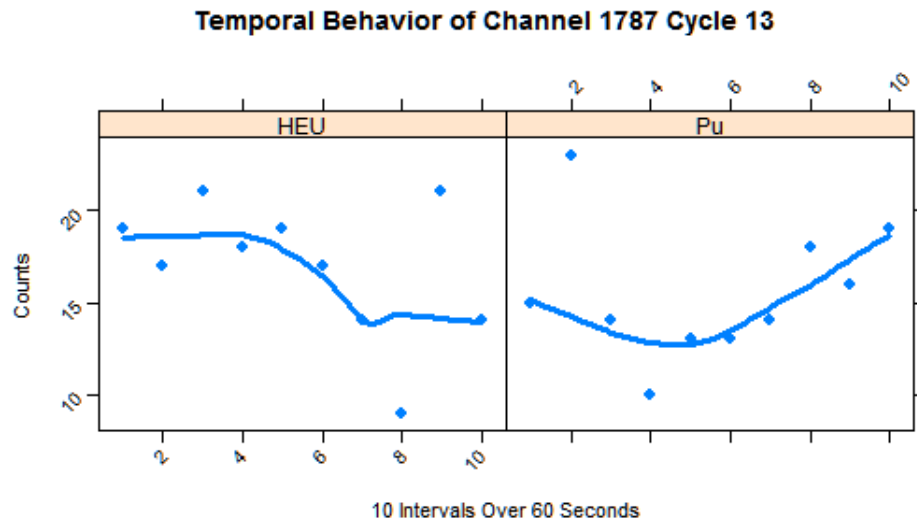


Figure 65: Channel 1787 Cycle 13 has a $\rho_{s,HEU}$ of -0.34, a $\rho_{s,Pu}$ of 0.75 and a $\Delta\rho_{s,HEU,Pu}$ of 1.09.

Template 4 identified several channels that were also identified by Templates 1 and 2. They were evaluated under Template 4 since their cycle frequency was below the 80 % threshold selected for Templates 1 and 2; however, they only showed up in at least 30 % of the cycles for Template 4. This was most likely due to the fact that this template was a hybrid of the decay and ingrowth templates. Template 4 was still able to identify channels that showed significant difference in temporal behavior; however, like Template 3 they were not seen consistently enough across the twenty cycles to be used as a model for identification of a sample of unknown SNM.

The proof-of-concept for this research involved evaluating single channels of the temporal spectra of uranium and plutonium. It should be noted that the resolution of the HPGe detector is such that evaluation of individual channels implies a better resolution than is actually achievable in traditional gamma-ray spectroscopy. Performing the same methods as outlined in this work on a range of channels (ie: grouping of 3 channels) may result in a more accurate representation of the resolution of the HPGe detector used and should be considered for future work.

As discussed earlier, Templates 1 and 2 showed the greatest consistency in identifying channels that showed significant differences between plutonium and uranium. Templates 3 and 4 did not identify channels that occurred with the same consistency across cycles. For this research, a one minute counting time was used which might not provide enough time to see the combination of ingrowth and decay patterns displayed by Templates 3 and 4. It would be beneficial to experiment with other counting times using these templates to see if they are able to identify channels

more consistently.

From the rules created through the supervised machine learning process, channels identified were those that displayed the greatest difference between plutonium and uranium, highlighting channels that displayed opposite trends (ingrowth or decay). The channels with the greatest consistency across twenty cycles were all located below 1 MeV. Channels displaying decay of both uranium and plutonium were not identified for this research and was a potential reason for the identification of channels below 1 MeV as the short-lived fission products at higher energies were decaying quickly for both materials.

Based on the results from Templates 1 and 2, seven channels were identified as displaying significant differences in temporal behavior for plutonium and highly enriched uranium. Furthermore, these channels showed up consistently in at least 80 % of the cycles. The channels were closely grouped (139 and 140; 301 and 302; 964 and 965) implying that a peak was most likely present at these locations in the spectrum. From this research, seven channels were identified which make up a model that could potentially be used for the identification of unknown special nuclear material.

4 Conclusion

Currently, most NDA techniques rely on the evaluation of the delayed gamma-ray spectrum at higher energies (≥ 3 MeV). The use of temporal gamma-ray spectrometry has been shown to identify and quantify special nuclear material within an uncertainty of 2 % at these higher energies. Building off of this research, the temporal gamma-ray spectroscopy method was combined with machine learning techniques to evaluate the spectrum below 3 MeV. Channels with significant attributes were identified through the use of Spearman's rank-order correlation coefficient. This metric was used to determine a set of rules that could be used to create a model for the potential identification and future quantification of plutonium-239 and uranium-235.

While all four templates were able to identify channels that highlighted the differences between plutonium and uranium, only Templates 1 and 2 were able to identify channels with enough consistency to be used to create a model and combined with other machine learning techniques for future identification and possible quantification of fissile material. Templates 1 and 2 identified seven channels that were present within at least 80 % of the cycles. These channels highlight the differences in the temporal spectra below 3 MeV, indicating that this method is able to identify useful information within otherwise complex data spectra.

5 Future Work

Focus was placed on evaluating the spectra of U-235 and Pu-239 since these materials are of greatest concern in the nuclear industry for nuclear safeguards. The methods discussed for the initial proof-of-concept of this research, successfully identified differences between fissile material. However, there are several areas that should be considered for future work before this method can be implemented and used for identification and quantification of special nuclear material with the same accuracy and precision seen with previous temporal spectrometry methods.

A 1 minute irradiation/counting cycle was used for this research. Data was also collected for 10 second and 10 min irradiation/counting cycles. As discussed previously, Templates 3 and 4 identified channels with less consistency than Templates 1 and 2. This could be due to the time scale at which the channels were evaluated. Since the time scale is relatively short, there might not be enough time for the fission decay products to exhibit the Template 3 and 4 patterns (ingrowth followed by decay or decay followed by ingrowth). By optimizing the count time, Templates 3 and 4 might be able to more consistently identify channels which would provide useful information for identification purposes. In addition, optimization of the count/rest time may reduce build-up seen across the twenty cycles.

Further evaluation of cycle consistency could also prove to be beneficial. In this research, channels were selected as significant if they showed up consistently in the twenty cycles. For Templates 1 and 2 channels that showed up in at least 80 %

of the cycles were identified as significant. However, the same cycle consistency was not seen for Templates 3 and 4. Channels identified by these templates showed up at most in 50 % of the cycles however, majority of these channels showed up in only 30 % of cycles. Further work needs to be done in order to determine what frequency percentage is necessary for a channel to be deemed as significant and incorporated into the model to be used as a profile.

Using a range of channels rather than evaluating the spectrum by single channels may also be beneficial. As mentioned previously, the current method evaluated individual channels of the spectrum. HPGe detectors have an energy resolution of about 1.7 keV. While looking at individual channels was successful for proof-of-concept, it implies the detector has a better energy resolution than exists. Therefore, it is suggested that ranges of 3 and 5 channels are evaluated.

The frequency quantile was chosen based on a unique selection for each cycle while ensuring that the minimum 100 count threshold was met. Evaluating the impact of implementing a frequency quantile selection of a standard 100 count threshold for all cycles could be useful. The current method led to a few cycles requiring a more restrictive quantile to be chosen. Studying the impact that this has on the other cycles could be important in further development and fine tuning of this method.

It was seen in the results and analysis section that the 95 % $\Delta\rho_{s,HEU,Pu}$ quantile was the best choice for channel identification. However, since a $\Delta\rho_{s,HEU,Pu}$ threshold was unique to the cycle and template, the lowest $\Delta\rho_{s,HEU,Pu}$ quantile allowed was 0.59. The average $\Delta\rho_{s,HEU,Pu}$ quantile was about 0.70; however, the channels that

showed up most consistently for Templates 1 and 2, had a minimum $\Delta\rho_{s,HEU,Pu}$ of 0.80. If a specific $\Delta\rho_{s,HEU,Pu}$ threshold value could be determined for all templates, a standard $\Delta\rho_{s,HEU,Pu}$ quantile could be used rather than a quantile that is unique to each cycle and template. Further evaluation of the $\Delta\rho_{s,HEU,Pu}$ score and its impacts on the $\Delta\rho_{s,HEU,Pu}$ quantile would be beneficial.

Using additional machine learning techniques to explore the combinations of individual ρ_s and the $\Delta\rho_{s,HEU,Pu}$ scores could also be beneficial. Currently, channels were selected as significant if they had a large $\Delta\rho_{s,HEU,Pu}$ value and the signs of individual ρ_s were opposite of one another. There are many combinations of individual ρ_s that yield high $\Delta\rho_{s,HEU,Pu}$ values. This creates a new complex data set that could benefit from machine learning techniques to further hone in on which channels are best to use as fingerprints in the identification of SNM.

Lastly, in this research it was shown that the seven channels identified high-light differences between plutonium and highly enriched uranium and may be useful for creating a profile to identify fissile material. It would be advantageous to also create profiles that could be used to identify a mixed sample of unknown SNM. Therefore, the evaluation of various mixtures of these materials using the same machine learning methods should also be performed (ie: 0/100, 50/50, 100/0).

References

- Avery, M. (1996). *Literature Review for Local Polynomial Regression*. Ph. D. thesis, North Carolina State University.
- Beddingfield, D. H. and F. E. Cecil (1998). Identification of fissile materials from fission product gamma-ray spectra. *Nuclear Instruments and Methods in Physics Research A* 417.
- Brase, Charles, Brase, C. (1983). *Understandable Statistics* (Second ed.). D.C. Heath and Company.
- Breiman, L. (2001). Breiman's Two Cultures paper.pdf. *Statistical Science* 16(3), 199–215.
- Charlton, W. (2011). Next Generation Safeguards Initiative Spent Fuel Effort External Review Committee: Final Report. Technical report, Washington: National Nuclear Security Administration.
- Chivers, D. H., K. Alfonso, B. L. Goldblum, and B. Ludewigt (2011). Nuclear Instruments and Methods in Physics Research B Novel methodology for the quantitative assay of fissile materials using temporal and spectral b -delayed c -ray signatures. *Nuclear Inst. and Methods in Physics Research, B* 269, 1829–1835.
- Dragovic, S. and Onjia, A. and Stankovic, S. and Anicin, I. and Bacic, G. (2005). Artificial neural network modelling of uncertainty in gamma-ray spectrometry. *Nuclear Instruments and Methods in Physics Research A* 540, 455–463.

- England, T. R., Rider, B. (1994). Evaluation and Compilation of Fission Product Yields. Technical report, Los Alamos National Laboratory.
- Firestone, R. B., G. A. English, J. Reijonen, F. Gicquel, K.-n. Leung, D. L. Perry, G. Garabedian, B. Bandong, Z. Révay, and G. L. Molnár (2005). Analysis of fissile materials by high-energy neutron-induced fission decay gamma-rays. *Journal of Radioanalytical and Nuclear Chemistry* 265(2), 241–245.
- Gozani, T. (1981). Active Nondestructive Assay of Nuclear Materials. Technical report, U.S Nuclear Regulatory Commission, Washington, DC.
- Gozani, T. (2009). Fission signatures for nuclear material detection. *IEEE Transactions on Nuclear Science* 56(3), 736–741.
- Hall, J. M., S. Asztalos, P. Biloft, J. Church, M. Descalle, T. Luu, and D. Manatt (2007). The Nuclear Car Wash : Neutron interrogation of cargo containers to detect hidden SNM q. *Nuclear Instruments and Methods in Physics Research B* 261, 337–340.
- Hata, H., K. Yokoyama, Y. Ishimori, Y. Ohara, Y. Tanaka, and N. Sugitsue (2015). Application of support vector machine to rapid classification of uranium waste drums using low-resolution γ -ray spectra. *Applied Radiation and Isotopes* 104, 143–146.
- IAEA (1970). Treaty on the Non-Proliferation of Nuclear Weapons. Technical report, Vienna: International Atomic Energy Agency.

- Kangas, L. J., P. E. Keller, E. R. Siciliano, R. T. K. Å, and J. H. Ely (2008). The use of artificial neural networks in PVT-based radiation portal monitors. *Nuclear Instruments and Methods in Physics Research A* 587, 398–412.
- King, R. D., S. Muggleton, R. a. Lewis, and M. J. Sternberg (1992). Drug design by machine learning: the use of inductive logic programming to model the structure-activity relationships of trimethoprim analogues binding to dihydrofolate reductase. *Proceedings of the National Academy of Sciences of the United States of America* 89(23), 11322–11326.
- Knoll, G. F. (2010). *Radiation Detection and Measurement* (Fourth ed.). Ann Arbor, MI: John Wiley & Sons, Inc.
- Little, R. C., M. B. Chadwick, and W. L. Myers. Detection of Highly Enriched Uranium Through Active Interrogation. Technical report, Los Alamos National Laboratory.
- Marrs, R. E., E. B. Norman, J. T. Burke, R. A. Macri, H. A. Shugart, E. Browne, and A. R. Smith (2008). Nuclear Instruments and Methods in Physics Research A Fission-product gamma-ray line pairs sensitive to fissile material and neutron energy. *Nuclear Instruments and Methods in Physics Research A* 592, 463–471.
- Miller, T. M., B. W. Patton, B. R. Grogan, J. J. Henkel, B. D. Murphy, J. O. Johnson, and J. T. Mihalczo (2013). Investigations of active interrogation techniques to detect special nuclear material in maritime environments: Standoff interrogation of

- small- and medium-sized cargo ships. *Nuclear Instruments and Methods in Physics Research, Section B: Beam Interactions with Materials and Atoms* 316, 94–104.
- Mukaka, M. (2012, sep). Statistics corner: A guide to appropriate use of correlation coefficient in medical research. *Malawi medical journal : the journal of Medical Association of Malawi* 24(3), 69–71.
- Norman, E. B., S. G. Prussin, R.-m. Larimer, H. Shugart, E. Browne, A. R. Smith, R. J. McDonald, H. Nitsche, P. Gupta, M. I. Frank, and T. B. Gosnell (2004). Signatures of fissile materials : high-energy g rays following fission. *Nuclear Instruments and Methods in Physics Research A* 521, 608–610.
- Oregon State University (2007). Safety Analysis Report for the Conversion of the Oregon State TRIGA from HEU to LEU Fuel.
- ORTEC (2016). DSPEC Pro Advanced, Digital Gamma-Ray Spectrometer for HPGe Detector Systems.
- Parker, H. M. O. and M. J. Joyce (2015). The use of ionising radiation to image nuclear fuel: A review. *Progress in Nuclear Energy* 85, 297–318.
- Reilly, Doug, Ensslin, Norbert, Smith, H. (1991). Passive Nondestructive Assay of Nuclear Materials. Technical report, Los Alamos National Laboratory.
- Robinson, J. (2012). *Design, Construction, and Characterization of a Neutron Depth Profiling Facility at the Oregon State University TRIGA Reactor with an Advanced Digital Spectroscopy System*. Ph. D. thesis, Oregon State University.

- Rodriguez, D. C., E. Anderson, K. K. Anderson, L. W. Campbell, J. E. Fast, K. Jarman, J. Kulisek, C. R. Orton, R. C. Runkle, and S. Stave (2013). Measurement and analysis of gamma-rays emitted from spent nuclear fuel above 3 MeV. *Applied Radiation and Isotopes* 82, 181–187.
- Sheskin, D. (2004). *Handbook of Parametric and Nonparametric Statistical Procedures* (Third ed.). CRC Press.
- Shultis, Kenneth L., Faw, R. E. (2008). *Fundamentals of Nuclear Science and Engineering* (Second ed.). CRC Press Taylor and Francis Group.
- Slaughter, D. R., M. R. Accatino, A. Bernstein, and J. A. Church (2005). Preliminary results utilizing high-energy fission product c -rays to detect fissionable material in cargo. *Nuclear Instruments and Methods in Physics Research B* 241, 777–781.
- Tobin, S.J., Sandoval, N.P., Fensin, M.L., Lee, S.Y, Ludewigt, B.A., Menlove, H.O., Quiter, B.J., Rajasingum, A., Schear, M.A., Smith, L.E., Swinhoe, M.T., Thompson, S. (2010). Determination of Plutonium Content in Spent Fuel with Nondestructive Assay. Technical report, Lawrence Berkeley National Laboratory.
- Varley, A., A. Tyler, L. Smith, P. Dale, and M. Carlo (2015). Development of a neural network approach to characterise ^{226}Ra contamination at legacy sites using gamma-ray spectra taken from boreholes. *Journal of Environmental Radioactivity* 140, 130–140.
- Varley, A., A. Tyler, L. Smith, P. Dale, and M. Davies (2016). Science of the Total

- Environment Mapping the spatial distribution and activity of ^{226}Ra at legacy sites through Machine Learning interpretation of gamma-ray spectrometry data. *Science of the Total Environment, The 545-546*, 654–661.
- Venables, W. N., D. M. Smith, and R Core Team (2016). An Introduction to R. *User Manual 2*, 99.
- Wei, W., Q. Du, and N. H. Younan (2010). Particle swarm optimization based spectral transformation for radioactive material detection and classification. *2010 IEEE International Conference on Computational Intelligence for Measurement Systems and Applications*, 1–6.
- Williford, R. (2013). *Temporal Gamma-Ray Spectrometry to Quantify Relative Fissile Material Content*. Ph. D. thesis, Oregon State University.
- Yoshida, E., K. Shizuma, S. Endo, and T. Oka (2002). Application of neural networks for the analysis of gamma-ray spectra measured with a Ge spectrometer. *Nuclear Instruments and Methods in Physics Research A 484*, 557–563.

